TWO-DIMENSIONAL DYNAMIC STALL AS SIMULATED IN A VARYING FREESTREAM

By

G. Alvin Pierce
Donald L. Kunz
John B. Malone

Prepared for

NATIONAL AERONAUTICS AND SPACE ADMINISTRATION
Langley Research Center
Grant No. NGR 11-002-185
Charles Eugene Hammond, Technical Officer

GEORGIA INSTITUTE OF TECHNOLOGY
SCHOOL OF AEROSPACE ENGINEERING
ATLANTA, GEORGIA 30332

TWO-DIMENSIONAL DYNAMIC STALL AS SIMULATED IN A VARYING FREESTREAM

By

G. Alvin Pierce

Donald L. Kunz

and

John B. Malone

Prepared by

GEORGIA INSTITUTE OF TECHNOLOGY

SCHOOL OF AEROSPACE ENGINEERING

Atlanta, Georgia 30332

Prepared for

NATIONAL AERONAUTICS AND SPACE ADMINISTRATION

Langley Research Center

Grant No. NGR 11-002-185

Charles Eugene Hammond, Technical Officer

ABSTRACT

A low speed wing tunnel equipped with an axial gust generator to simulate the aerodynamic environment of a helicopter rotor was used to study the dynamic stall of a pitching blade. The objective of this investigation was to find out to what extent harmonic velocity perturbations in the freestream affect dynamic stall. The study involved making measurements of the aerodynamic moment on a two-dimensional, pitching blade model in both constant and pulsating airstreams. Using an operational analog computer to perform on-line data reduction, plots of moment versus angle of attack and work done by the moment were obtained. The data taken in the varying freestream were then compared to constant freestream data and to the results of two analytical methods. These comparisons showed that the velocity perturbations had a significant effect on the pitching moment which could not be consistently predicted by the analytical methods, but had no drastic effect on the blade stability.

TABLE OF CONTENTS

LIST OF TABLES

LIST OF FIGURES

SYMBOLS

C_m	aerodynamic moment coefficient
R	model frequency/freestream frequency
Re	Reynolds number based on semichord
V	freestream velocity
$\bar{V}$	mean freestream velocity
V'	amplitude of freestream velocity fluctuation
V_r	relative mean freestream velocity identified in Figure 13
V_∞	constant freestream velocity
α	angle of attack
$\dot{\alpha}$	angular velocity
$\ddot{\alpha}$	angular acceleration
$\bar{\alpha}$	mean angle of attack
α'	amplitude of angle of attack
ϕ	freestream velocity phase angle identified in Figure 13
$\Delta\phi$	velocity phase-angle range for one cycle of airfoil motion
ϕ_m	mean velocity phase angle for one cycle of airfoil motion

ω_v frequency of freestream velocity fluctuation

ω_α frequency of angle of attack

TWO-DIMENSIONAL DYNAMIC STALL AS SIMULATED IN A VARYING FREESTREAM

by

G. Alvin Pierce, Donald L. Kunz, and John B. Malone

Georgia Institute of Technology

Atlanta, Georgia

INTRODUCTION

The dynamic or transient stall of lifting surfaces has long been recognized as a very complex non-linear aerodynamic phenomenon. It has been experienced by fixed-wing aircraft during abrupt maneuvers and gust impingement, by compressor rotors during off-design conditions, and by helicopter rotors on the retreating blade. The importance of transient stall to the structural designer appears as an aerodynamic loading in excess of that predicted under static conditions. In the case of dynamic stall when the surface is oscillating, it has been observed that for certain conditions a hysteretic load reaction is developed which can be destabilizing. This is of great importance to the aeroelastician since it may cause a structural dynamic instability known as stall flutter.

The primary concern of this report is the nature of the oscillatory dynamic stall as experienced by a retreating helicopter blade. Numerous experimental investigations have been conducted (References 1-12) to determine both the detailed nature of the stall phenomenon and the resulting aerodynamic reactions on the lifting surface. These studies have incorporated flow visualization techniques, pressure-plotting time histories, normal-force and pitching-moment measurements, and structural-dynamic transient-response recordings. Most of these efforts have been very comprehensive and quite informative, but they were all performed in a uniform airstream, which does not simulate the true rotor environment.

Stall flutter as experienced by a retreating blade of a helicopter rotor occurs while the local airspeed is rapidly changing. Since it has

been thoroughly established (References 5, 13, 14) that dynamic stall is characterized by discrete vortex shedding, the net loads on the airfoil must be strongly influenced by the proximity of the shed vortices. The propagation of these vortices into the wake is in part determined by the local airspeed. Therefore it can be concluded that the rapidly changing local airspeed of the retreating blade could have a significant effect on the unsteady aerodynamic loads. As a consequence of this observation it was felt that there is a definite need for an experimental investigation to establish the influence of a non-uniform airstream on the aerodynamic reactions during dynamic stall.

It may be noted that in addition to the experimental investigations previously cited there have been numerous parallel efforts (References 10, 15-20) to either empirically or analytically predict the air loads during dynamic stall. These studies in all cases have restricted their attention to the condition of a uniform airstream. Although such predictions may satisfactorily agree with the experimental measurements, they most certainly do not incorporate the effects of the locally varying airspeed.

This report discusses an experimental investigation (References 21-22) which was conducted in a low speed wing tunnel. The tunnel had been modified to generate simple harmonic perturbations in the freestream airspeed. A two-dimensional airfoil model was oscillated in pitch about various mean angles of attack near the static stall condition. The resulting unsteady pitching moment is correlated with the instantaneous angle of attack and integrated to establish its influence on dynamic stability.

WIND TUNNEL FACILITY

This investigation was carried out in the Georgia Tech Low Turbulence Wind Tunnel (Figure 1). The wind tunnel which is of the closed-jet open-circuit type has a maximum airspeed of 80 feet per second in the test section. Downstream of the fan and upstream of the converging nozzle is a honeycomb screen which serves to straighten the flow and to limit the size of the turbulent eddies. One sidewall of the test-section is fitted with screw-jacks so that the test-section contour can be varied. For this investigation the sidewalls were parallel, which provided a square test-section, 42 inches on a side.

Gust Generator

The gust generator (Figure 2) is located at the downstream exit of the wind tunnel. This mechanism consists of four component systems: the drive motor and controls, the drive-side gear box, the idle-side assembly, and the vanes. The power source for the gust generator is a Wood's, one horsepower, SCR motor. A Wood's Model U-100 ULTRACON drive control regulates the motor torque and speed. A pulley and belt drive transfers the rotational motion of the motor shaft to the drive-side gear box.

Power is transmitted from the motor to the vanes through this drive-side gear box which contains a worm gear, a vertical shaft, and a series of bevel gears and slotted shafts set in pillow blocks. Horizontal rotation from the motor is geared down and changed to vertical rotation through the worm gear. The vertical shaft transfers the rotation to the vanes through the bevel gears, which change the vertical rotation back to horizontal rotation. Six slotted shafts serve as points of attachment for the vanes.

On the other side of the wind tunnel is the idle-side assembly. The main components of this assembly are six slotted shafts, each set in a pair of pillow blocks. Mounted on the second shaft from the bottom are the vane RPM gear and timing disk. The vane RPM gear is a 60-tooth gear which was used in conjunction with a magnetic pickup, filter, and

electronic counter, to determine the rotational rate of the vanes. The timing disk, which is an aluminum disk with a steel stud set into the edge, was used together with a magnetic pickup to give a voltage pulse at a specific point in the vane rotation.

The vanes of the gust generator are made from 1/4 inch thick aluminum, 42 inches long, and of different widths, depending on the percent blockage desired. At each end, along the centerline, are holes through which the vanes are bolted to the slotted shafts which protrude into the wind tunnel. Vane widths are designated by how much of the wind tunnel exit area is blocked off when the vanes are in a vertical position. For example, the set of 70 percent vanes blocks off 70 percent of the tunnel exit area. In order to minimize flow angularity in the test section, adjacent vanes rotate in opposite directions.

A description of the gust generator calibration and resulting data are presented in Reference 21. Figure 3 shows the operational limits of the gust generator for the 30, 50, and 70 percent vanes between 0.67 and 2 Hertz. It should be pointed out that as the gust frequency increases, for a constant mean velocity, the gust amplitude decreases. Thus, the upper limit gust amplitude curve for each set of vanes represents a frequency of 0.67 Hertz, while the lower limit represents a frequency of 2 Hertz. The upper and lower limits on mean velocity were determined by where the waveform began to appreciably deviate from being simple harmonic.

Since there is no point where any of the operational limits overlap, it is impossible to vary one parameter (gust frequency, amplitude, or mean velocity) and hold the other two constant. With this in mind, and wanting to retain only a few significant variables, it was decided to select one mean velocity and one set of vanes for all the tests. Using the 50 percent vanes and a mean velocity of 42.50 feet per second, gust amplitudes of 7.53 and 3.04 feet per second were obtained at 1 and 2 Hertz respectively (Table 1).

Hot-wire Anemometer

Velocity measurements in the wind tunnel were made with a hot-wire anemometer. This means of measurement was selected for its accuracy, ease of use, and voltage output. The model used was a Flow Corporation Model 900-A constant-temperature hot-wire anemometer. The probe, also made by Flow Corporation, was 14 inches long and 1/4 inch in diameter. A piece of 0.00035 inch diameter tungsten wire, welded to the probe tip, served as the sensing element. With this arrangement, it was possible to measure velocities of less than one foot per second.

Calibration of the hot-wire was accomplished in the wind tunnel using the anemometer and probe, a manometer, and a pitot-static probe. The hot-wire probe was placed in the position where it was to be during the tests, while the pitot-static probe was located in a downstream position. In these locations, neither probe appeared to interfere with the other. With the wind off, the manometer and pitot probe were connected, and the manometer adjusted to read a column height of zero. After turning the wind tunnel on the hot-wire probe element was oriented perpendicular to the flow direction by rotating the probe until the maximum output was obtained. For constant wind tunnel velocities between 5 and 70 feet per second, the manometer height and hot-wire voltage were recorded. In addition, the average stagnation temperature and stagnation pressure were determined over the duration of the calibration run.

Reduction and curve fitting for this data was done on a digital computer. The program converted manometer column height to velocity using the incompressible Bernoulli equation, then fit both linear and quadratic curves to the data by a least squares approximation. Using the standard deviation of each curve, the better fit was selected as the calibration curve. The curve fit used throughtout this part of the investigation is illustrated in Figure 4.

MODEL AND DRIVE MECHANISM

Airfoil Model and Support

The model used in these tests was constructed from balsa blocks, which were laminated together and bonded to a 7/8 inch diameter steel spar. The blocks were shaped into a 9 inch chord, NACA 0012 contour that had a 42 inch span. The spar was located at the quarter-chord. After the shaping was complete, the model surface was sealed and painted. To mass balance the model, two rectangular, brass bars were attached to the spar. The locations for the bars were such that when the model was installed in the wind tunnel, the bars were outside the test-section walls. Thus, the airflow inside the tunnel was not disturbed.

An accelerometer to detect transverse motion was installed at a point 2.5 inches aft of the axis of rotation. It was located near the edge of the model, next to the wall of the test-section. In this location, the aerodynamic disturbances created by the accelerometer would have a minimum effect on the overall flow pattern.

Due to the requirement that all supports be free of the test-section walls, both supports for the model suspension system were attached to the external wind tunnel structure. On the side where the oscillating mechanism was installed, the support structure consisted of a base plate bolted to the tunnel with steel angles. On the other side, the support was a trapezoidal frame constructed of steel angles.

The model suspension system which consisted of two main bearing assemblies (Figure 5), were located outside and on either side of the test section. The center arm on each assembly was pinned to the base at one end and fixed at the other. Strain gage bridges were bonded to the center arm at the points where the arm had been milled down to facilitate the measurement of lift.

Oscillating Mechanism

The oscillating mechanism for the model (Figures 6 and 7) was designed so that mean angle of attack, amplitude of oscillation, and frequency could all be varied. The driving element for this system was an interchangeable eccentric drive which was powered by a Minarik, 1/2

horsepower, shunt motor. A Model WTF-73, Minarik Tachometer Generator regulated the motor speed. The oscillatory frequency was measured in the same manner as the vane frequency, using a 60-tooth gear, magnetic pickup, low-pass filter, and electronic counter.

The eccentric drive transformed the rotational motion of the motor shaft into the oscillatory motion of the model. It was fixed to the motor shaft, and had an off-center crank pin to which the drive rod was connected. The distance that the crank pin was away from the center determined the amplitude of oscillation. Although four different eccentrics were available ($\pm 2^\circ$, $\pm 4^\circ$, $\pm 6^\circ$, $\pm 8^\circ$), only the $\pm 4^\circ$ drive was used.

The drive arm and drive rod assembly (Figure 8) transferred the motion of the eccentric to the model spar. As the drive arm oscillated the linkage shaft, the motion was transmitted to the model spar through the angle-of-attack adjustment disks. By changing the relative positions of the disks, the mean angle of attack of the model could be varied.

Transducers

A strain gage bridge was bonded onto the drive arm (Figure 8). This bridge detected a signal proportional to the total moment on the model. The calibration curve for the bridge is shown in Figure 9.

Since no quantitative measurement of acceleration was required in this investigation, the B & K Model No. 306 accelerometer that was attached to the model was not calibrated. Its signal was used, however, in the synthesis of an angle-of-attack scale, and to cancel out the output of the moment strain bridge as the model oscillated in still air. These procedures will be explained in a later section.

DATA ACQUISITION AND REDUCTION

Acceleration and Moment

Both the acceleration signal from the model accelerometer and the total moment signal from the drive arm strain gage bridge contained an appreciable amount of high frequency noise. These unwanted disturbances were eliminated by processing the data (Figure 10) with a low-pass Krohn-Hite filter which only passed frequencies below 20 Hertz. Although these filters did not distort the basic signals, they did introduce a phase shift. A subsequent phase adjustment was accomplished by passing the acceleration signal through a Spectral Dynamics narrow bandwidth tracking filter. These measured data were then inputed to an analog computer.

Aerodynamic Moment

Before the aerodynamic moment data could be identified, all components of the measured moment not due to the air loads had to be eliminated. This was accomplished on an Electronic Associates TR-48 operational analog computer with a DES-30 parallel logic unit. The process consisted of minimizing the calibrated total moment signal during wind-off operation of the tunnel by subtracting signals proportional to inertial moment, damping moment, and higher-order contributions.

The analog mechanization which converted the total moment signal to aerodynamic moment is illustrated in Figure 11. The total moment signal on Trunk 3 is modified by the bridge calibration data prior to being fed into Amplifier A09, where the correction factors are applied. The first correction is an inertial term which is proportional to the angular acceleration of Trunk 2. This signal is multiplied by an appropriate gain to minimize the output of A09.

The damping correction is proportional to the angular velocity, which is the integral of the acceleration. Since open-loop integration on an analog computer is normally an unstable operation, it was necessary to use an integration stabilization circuit. The stabilization circuit is an error feedback system in which the sum of the relative maxima and minima of the integrated signal are fed back into the integrator. In

this case, the angular velocity of integrator I11 provides the inputs for track-and-store units which are controlled by Comparator C21. This comparator is driven by the angular acceleration which is 90° out of phase with the desired angular velocity. Having obtained a stable angular velocity, an optimum gain was applied to the output of A07 to again minimize the A09 output.

An oscilloscope display of the corrected moment versus angular acceleration indicated that although the $\dot{\alpha}$ and $\ddot{\alpha}$ corrections had removed most of the wind-off moment contributions, some still remained. The most obvious high-order correction needed was an $\ddot{\alpha}^2$ term. The angular acceleration was squared (Figure 12) and applied to the total moment in A09. Viewing the moment with three correction terms, versus angular acceleration on an oscilloscope, indicated the need for an $\dot{\alpha}\,\ddot{\alpha}$ factor. Multiplication of the angular velocity by the angular acceleration was accomplished by an electronic multiplier on the computer. This term was adjusted to yield a minimum output from amplifier A09 for the wind-off condition.

The gains on the correction inputs to A09 indicate that the $\dot{\alpha}$ and $\ddot{\alpha}$ contributions amounted to the greater part of the moment acting on the model, while it oscillated in still air. Even though $\ddot{\alpha}^2$ and $\dot{\alpha}\,\ddot{\alpha}$ contributions were approximately an order of magnitude smaller than the $\dot{\alpha}$ and $\ddot{\alpha}$ contributions, they were still very important since they were of the same order of magnitude as the measured aerodynamic moment. These results are presented as aerodynamic coefficients which are nondimensionalized with respect to the mean freestream dynamic pressure, model area and chord.

Data Recording

The aerodynamic moment coefficient was presented on an oscilloscope versus a synthesized angle of attack. Since the filtered model acceleration signal was a simple harmonic function of time it was exactly 180° out of phase with angle of attack. Consequently the synthesized angle of attack was taken as the filtered acceleration times an appropriate gain.

These oscilloscope traces of moment versus angle of attack were then photographed with a camera which was equipped with an electronic shutter.

Since the frequency of the freestream velocity fluctuations was significantly lower than the oscillatory frequency of the model, the recorded moment trace for a given cycle of model pitch oscillation corresponded to only a fraction of a velocity fluctuation cycle. The specific regions of the velocity cycle, during which the photographs were taken, were centered about the: mean increasing velocity (0°), maximum velocity (90°), mean decreasing velocity (180°), and minimum velocity (270°).

As an example, consider a model frequency 6 times the frequency of the velocity (Figure 13). Since one model pitching cycle would cover 60° of one velocity cycle, a photograph of the 90° region would start at 60° and end at 120°. Similarly a photograph of the 180° area would start at 150° and end at 210°. In Figure 13 the solid lines show the areas of the curve that correspond to each photograph.

With the equipment available, it was not possible to control the phase relationship between the velocity and model pitch oscillations. Thus, under otherwise identical conditions, the pitching cycle recorded for any particular region might begin and end at 0° one time and at 20° the next. This situation was monitored during the course of the tests, and was found to have no observable effect on the data.

To obtain these photographs it was necessary to generate a voltage pulse which was synchronized with the gust. This was accomplished by installing a timing disk on a vane shaft (Figure 14). Mounted on the edge of the disk was a steel stud which passed close to a magnetic transducer once every vane rotation (once every other velocity cycle). The transducer provided the pulse which could be synchronized with the desired gust-velocity phase angle by rotation of the disk. These pulses were processed by the logic unit of the analog computer (Figures 15 and 16) to provide the necessary triggering pulses for the camera shutter and oscilloscope sweep.

Aerodynamic Work

The work performed on the airfoil by the aerodynamic moment was determined on the analog computer. Positive values of this work, a clockwise locus of aerodynamic moment versus angle of attack, contributed a destabilizing effect on the airfoil motion. This work was determined by direct integration of the product of aerodynamic moment and angular velocity. The integrator output was processed by an accumulator circuit on the analog.

Average values of work per cycle of airfoil oscillation were determined over several cycles of freestream fluctuation. The analog computer circuit was used to sum the individual values of work per cycle. Then, the final accumulator output was divided by the total number of cycles of airfoil oscillation to obtain a voltage which represented the average of work per cycle.

When the work over any one cycle of pitching oscillation was positive, that cycle was considered to be unstable. Strong instabilities were indicated by large values of positive work. Stable oscillations showed negative work, and the work for increasingly stable oscillations became more negative.

RESULTS

Static Moment Data

Figure 17 shows the static moment curve for the airfoil model. The data were taken at an airspeed of 42.50 ft/sec (Re 2.02×10^5), which was the mean velocity for all of the varying freestream conditions. Also shown in the figure is the static moment curve as presented by Carta et al. in Reference 10. It is apparent that although both models had an NACA 0012 cross-section, the moment curves are markedly different. The present data show a gradual increase in nose-down moment after a sharp dropoff, which indicates that this model underwent thin airfoil stall. Carta's moment curve shows a large increase in nose-down moment which continues out to an angle of attack of 24°. This behavior is typical of leading edge stall that would, in most cases, be associated with a 12% thick airfoil section.

This evaluation of the two static curves is verified by the findings of Gault in Reference 23, and Ericsson and Reding in Reference 24. They pointed out that the type of stall is strongly dependent on both Reynolds number and leading edge curvature. For a Reynolds number of 1.03×10^6 as Carta had, it would be expected that the airfoil would normally experience leading edge stall, as indicated in Figure 18 from Reference 23. Depending on such factors as surface roughness and turbulence, there is also the possibility that the stall could be of the mixed leading and trailing edge type. The findings in Reference 23 indicate that at a Reynolds number of 2.02×10^5 thin airfoil stall would be expected. These differences in static behavior suggest that there might also be differences in dynamic behavior. There was no attempt made to modify the results of this investigation to account for these effects of Reynolds number.

Varying Freestream Effects

The specific conditions examined in this program to establish the effect of a varying freestream on dynamic stall are itemized in Table 2. All tests were performed at a mean airspeed ($\bar{V}$) of 42.50 ft/sec and an angle-of-attack amplitude (α') of 4°. The conditions were chosen

to best isolate the dependence of aerodynamic moment on mean angle of attack, model frequency, gust frequency, and the ratio of these frequencies. The notation of Table 2 is defined by the following expressions for angle of attack and freestream velocity.

$$\alpha = \bar{\alpha} + \alpha' e^{i\omega_\alpha t}$$

$$V = \bar{V} + V' e^{i\omega_V t}$$

$\Delta\phi$ represents the velocity phase-angle range for one cycle of airfoil motion as illustrated in Figure 13.

To isolate the effect of the fluctuating freestream, the aerodynamic moment is presented in Figures 19-25 for four mean phase angles of the varying freestream. Also illustrated on these figures are equivalent data as measured in a constant freestream at speeds which correspond to the relative mean velocities identified in Figure 13. In this manner it is possible to compare constant and varying freestream data in which only the dynamic effects of the freestream are present. It should be noted that all coefficients are based on the same mean freestream speed.

Holding all of the other parameters constant, the mean angle of attack was varied so that the model would oscillate about 6°, 10°, 14°, and 18°. Since the amplitude for all cases was 4°, the model was operating in four different regimes with respect to the static stall angle of approximately 11°. At a mean angle of 6° (Figure 19) the moment curves were nearly elliptical and the oscillations were stable. At a mean angle of attack of 10° a drastic change occurred in the moment curves as illustrated in Figure 20. A destabilizing moment appeared at the high and low angle of attack limits. These data are also characterized by a definite nose-down moment at the minimum angle. At 14° the moment became completely unstable at all angles as shown in Figure 21. There was also no significant distortion of the moment at the lower angles. Although the motion at 18° was unstable (Figure 22), it was somewhat

less unstable than that with a 14° mean angle.

An increase in model frequency had a profound effect on the shapes of the moment curves as seen by comparing Figures 20 and 23. By increasing the model frequency from 6 to 12 Hertz, while holding the model-to-gust frequency ratio constant, all traces of destabilizing effects were eliminated and the curves became nearly elliptical. This effect was verified by making similar comparisons with other cases. The effect of the model-to-gust frequency ratio is best illustrated by comparing Figures 20 and 24. In both cases the model frequency is 6 Hertz. The distorted moment curves are very similar except for a slight decrease in the destabilizing effect at the lower ratio in Figure 24.

In many of the moment loci in Figures 19-25, there exist discontinuities between the beginning and end of the cycles. In the varying freestream, this is to be expected because of the velocity fluctuations. However, in the constant freestream data similar discontinuities, which can serve as measures of experimental error, also appear. Another indication of the scatter in the data can be seen by comparing the constant freestream curves at 42.50 fps in Figures 20 and 24. For identical conditions, these curves differ in the size of the loops, but retain the same general character.

In contrast with the bulk of data in the literature, none of the curves in Figures 19-25 show a decrease in pitching moment coefficient as the angle of attack approaches its maximum. The reason for this is unknown, but the good repeatability of the data would indicate that these are not isolated anomalies.

The effect of the varying freestream is shown most clearly in Figures 20 and 24, where the moment loci change radically from the constant airspeed condition. It appears that the varying freestream causes the moment locus to lag the equivalent constant freestream data by approximately 90° of the gust cycle. This effect can be seen by rotating the positions of the four varying freestream plots by 90° in the counterclockwise direction. In this new position, nearly every curve matches the constant freestream data better than when they were in their original positions.

Because the other conditions were characterized by nearly elliptical moment curves, this effect is more difficult to observe. However, in every case tested, this phenomenon could be seen by comparing the areas inside the curves.

Analytical Comparisons

For both correlation and verification purposes it was desirable to compare the experimental results with methods offered by prior investigators. Two such methods are described below.

The first is the empirical scheme of Carta et al. published in Reference 10. In that presentation, tables of normal force and pitching moment coefficients are tabulated for an airfoil oscillating in a constant freestream. These tables were inputed to a computer program that could interpolate between the data points. This program was set up such that the stored data could be applied to harmonically varying freestreams, as well as constant freestreams.

The second is an analytical development by Greenberg in Reference 25, which is based on Theodorsen's treatment of unsteady potential flows (Reference 26). While Theodorsen treated the problem of an airfoil undergoing simple harmonic oscillations in a constant airstream, Greenberg expanded the problem to include a harmonically pulsating freestream velocity. This potential flow analysis was programmed for correlation with the current data.

The results of these two methods are compared with the measured data in Figures 26-32. In all cases the potential flow analysis of Greenberg predicts an elliptical moment as a function of angle of attack, while the Carta scheme provides a distorted curve. For the conditions of Figure 27 the correlation is only fair between the test results and the two predictive methods. At the higher mean angle of 18° in Figure 29 the Carta results compare very well with the measured data. At this high angle the potential analysis of Greenberg does not compare well as would be expected. For the high model frequency of Figure 30 it is seen that the experimental moment curve becomes nearly elliptical as predicted by the Greenberg analysis and previously observed.

Aerodynamic Work

The average integrated work per cycle which was performed by the aerodynamic moment is nondimensionalized into a work coefficient. This coefficient is based on the mean freestream dynamic pressure, the model area and chord. Work coefficients were measured for mean angles from 0° to 20° and several values of model-to-gust frequency ratio (R). The frequency ratio was varied by keeping the model frequency at a constant value of 10 Hertz and changing the gust frequency.

Figure 33 is typical of the data obtained. It illustrates the sensitivity of the destabilizing effect of the aerodynamic moment to the mean angle of oscillation. It is also quite apparent in the figure tnat the work coefficient is not very dependent on the frequency ratio. It can therefore be concluded that the dynamic effects of the varying freestream have very little influence on the destabilizing effect of the aerodynamic moment.

CONCLUSIONS

The following conclusions which are based on the results of this investigation pertain to a Reynolds number of 2.02×10^5. Some engineering discretion should be exercised in extending these observations to conditions of higher Reynolds numbers.

1. The varying freestream velocity has a significant effect on the unsteady aerodynamic moment for airfoil pitching oscillations in the vicinity of static stall.
2. For sinusoidal oscillations in angle of attack, the simple harmonic freestream velocity variations do not significantly increase the aerodynamic work done on the airfoil by the freestream.

REFERENCES

1. Halfman, R. L., H. C. Johnson and S. M. Haley, "Evaluation of High-Angle-of-Attack Aerodynamic Derivative Data and Stall Flutter Prediction Techniques," NACA TN 2533, 1951.

2. Rainey, A. G., "Measurement of Aerodynamic Forces for Various Mean Angles of Attack of an Airfoil Oscillating in Pitch and on Two Finite-Span Wings Oscillating in Bending with Emphasis on Damping in the Stall," NACA TN 3643, 1956.

3. Carta, F. O., "Experimental Investigation of the Unsteady Aerodynamic Characteristics of an NACA 0012 Airfoil," United Aircraft Research Laboratories Report M-1281-1, August 1960.

4. Ham, N. D. and M. I. Young, "Torsional Oscillation of Helicopter Blades Due to Stall," AIAA Journal of Aircraft, Vol. 3, No, 3, May-June 1966, pp. 218-224.

5. Ham, N. D. and M. S. Garelick, "Dynamic Stall Considerations in Helicopter Rotors," Journal of the American Helicopter Society, Vol. 13, No. 2, April 1968, pp. 49-55.

6. Liiva, J., F. J. Davenport, L. Gray and I. C. Walton, "Two-Dimensional Tests of Airfoils Oscillating Near Stall, Vol. I, Summary and Evaluation of Results," USAAVLABS TR 68-13A, U. S. Army Aviation Material Laboratories, Fort Eustis, Virginia, April 1968, AD 670957.

7. Gray, L., J. Liiva, and F. J. Davenport, "Wind Tunnel Tests of Thin Airfoils Oscillating Near Stall, Vol. 1: Summary and Evaluation of Results," USAAVLABS TR-68-89a, January 1969.

8. Isogai, K., "An Experimental Study of the Unsteady Behavior of a Short Bubble of an Airfoil During Dynamic Stall with Special Reference to the Mechanism of the Stall Overshoot Effect," MIT Aeroelastic and Structures Research Laboratory, ASRL TR 130-2, June 1970.

9. McCroskey, W. J. and R. K. Fisher, Jr., "Detailed Aerodynamic Measurements on a Model Rotor in the Blade Stall Regime," Journal of the American Helicopter Society, Vol. 16, No. 1, January 1971, pp. 20-30.

10. Carta, F. O., G. L. Commerford, R. G. Carlson, and R. H. Blackwell, "Investigation of Airfoil Dynamic Stall and Its Influence on Helicopter Control Loads," USAAMRDL Tech. Rep. 72-51, September 1972.

11. Philippe, J. J. and M. Sagner, "Calculation and Measurement of Aerodynamic Forces on an Oscillating Airfoil Profile with and without Stall," AGARD Conference Proceedings No. 111, Marseilles, September 1972.

12. Martin, J. M., R. W. Empey, W. J. McCroskey and F. X. Caradonna, "A Detailed Experimental Analysis of Dynamic Stall on an Unsteady Two-Dimensional Airfoil," presented at the 29th Annual National Forum of the American Helicopter Society, Washington, D.C., May 1973, Preprint No. 702.

13. Ham, N. D., "Stall Flutter of Helicopter Rotor Blades: A Special Case of the Dynamic Stall Phenomenon," Journal of the American Helicopter Society, Vol. 12, No. 4, October 1967, pp. 19-21.

14. Jones, W. P., W. J. McCroskey, and J. J. Costes, "Unsteady Aerodynamics of Helicopter Rotors," AGARD Report No. 595, October 1972.

15. Ham, N. D., "Aerodynamic Loading on a Two Dimensional Airfoil During Dynamic Stall," AIAA Journal, Vol. 6, No. 10, October 1968, pp. 1927-1934.

16. Liiva, J. and F. J. Davenport, "Dynamic Stall of Airfoil Sections for High-Speed Rotors," Journal of the American Helicopter Society, Vol. 14, No. 2, April 1969, pp. 26-33.

17. Ericsson, L. E. and J. P. Reding, "Unsteady Airfoil Stall," NASA CR-66787, July 1969.

18. Patay, J. A., "Leading Edge Separation on an Airfoil During Dynamic Stall," Mass. Inst. of Tech. Aeroelastic and Structures Research Laboratory, ASRL TR 156-1, October 1969.

19. Tarzanin, F. J., Jr., "Prediction of Control Loads Due to Blade Stall," Journal of the American Helicopter Society, Vol. 17, No. 2, April 1972.

20. Crimi, P. and B. L. Reeves, "A Method for Analyzing Dynamic Stall of Helicopter Rotor Blades," NASA CR-2009, May 1972.

21. Malone, J. B., "Dynamic Stall Characteristics of an Oscillating Airfoil in a Harmonically Varying Freestream Velocity," Ph.D. Dissertation, Georgia Institute of Technology, December 1974.

22. Kunz, D. L., "Unsteady Drag and Dynamic Stall as Simulated in a Varying Freestream," Ph.D. Dissertation, Georgia Institute of Technology, March 1976.

23. Gault, D. E., "A Correlation of Low-Speed, Airfoil-Section Stalling Characteristics with Reynolds Number and Airfoil Geometry," NACA TN 3963, March 1957.

24. Ericsson, L. E. and Reding, J. P., "Dynamic Stall Simulation Problems," Journal of Aircraft, Vol. 8, No. 7, July 1971, pp. 579-583.

25. Greenberg, J. M., "Airfoil in Sinusoidal Motion in a Pulsating Stream," NACA TN 1326, June 1947.

26. Theodorsen, T., "General Theory of Aerodynamic Instability and the Mechanism of Flutter," NACA Report 496, 1935.

Table 1. Gust Generator Operational Curves for the 50% Vanes (0.67 - 2 Hertz)

ω_v(Hz)	Gust Amplitude (fps)
0.67	$V' = -2.0180 + .1900\ \bar{V} + .0024\ \bar{V}^2$
0.83	$V' = -1.6940 + .1542\ \bar{V} + .0022\ \bar{V}^2$
1.00	$V' = -1.3440 + .1196\ \bar{V} + .0021\ \bar{V}^2$
1.17	$V' = -0.9690 + .0865\ \bar{V} + .0020\ \bar{V}^2$
1.33	$V' = -0.5685 + .0545\ \bar{V} + .0020\ \bar{V}^2$
1.50	$V' = -0.1425 + .0238\ \bar{V} + .0020\ \bar{V}^2$
1.67	$V' = 0.3089 - .0056\ \bar{V} + .0021\ \bar{V}^2$
1.83	$V' = 0.7858 - .0337\ \bar{V} + .0022\ \bar{V}^2$
2.00	$V' = 1.2880 - .0606\ \bar{V} + .0024\ \bar{V}^2$

Table 2. Oscillating Airfoil Experimental Flow Conditions

Figure No.	$\bar{\alpha}$(deg)	α'(deg)	ω_α(Hz)	$\bar{V}$(fps)	V'(fps)	ω_v(Hz)	R	$\Delta\phi$(deg)
19,26	6	4	6	42.50	7.53	1	6	60
20,27	10	4	6	42.50	7.53	1	6	60
21,28	14	4	6	42.50	7.53	1	6	60
22,29	18	4	6	42.50	7.53	1	6	60
23,30	10	4	12	42.50	3.04	2	6	60
24,31	10	4	6	42.50	3.04	2	3	120
25,32	10	4	12	42.50	7.53	1	12	30

$$\alpha = \bar{\alpha} + \alpha' e^{i\omega_\alpha t} \qquad V = \bar{V} + V' e^{i\omega_v t}$$

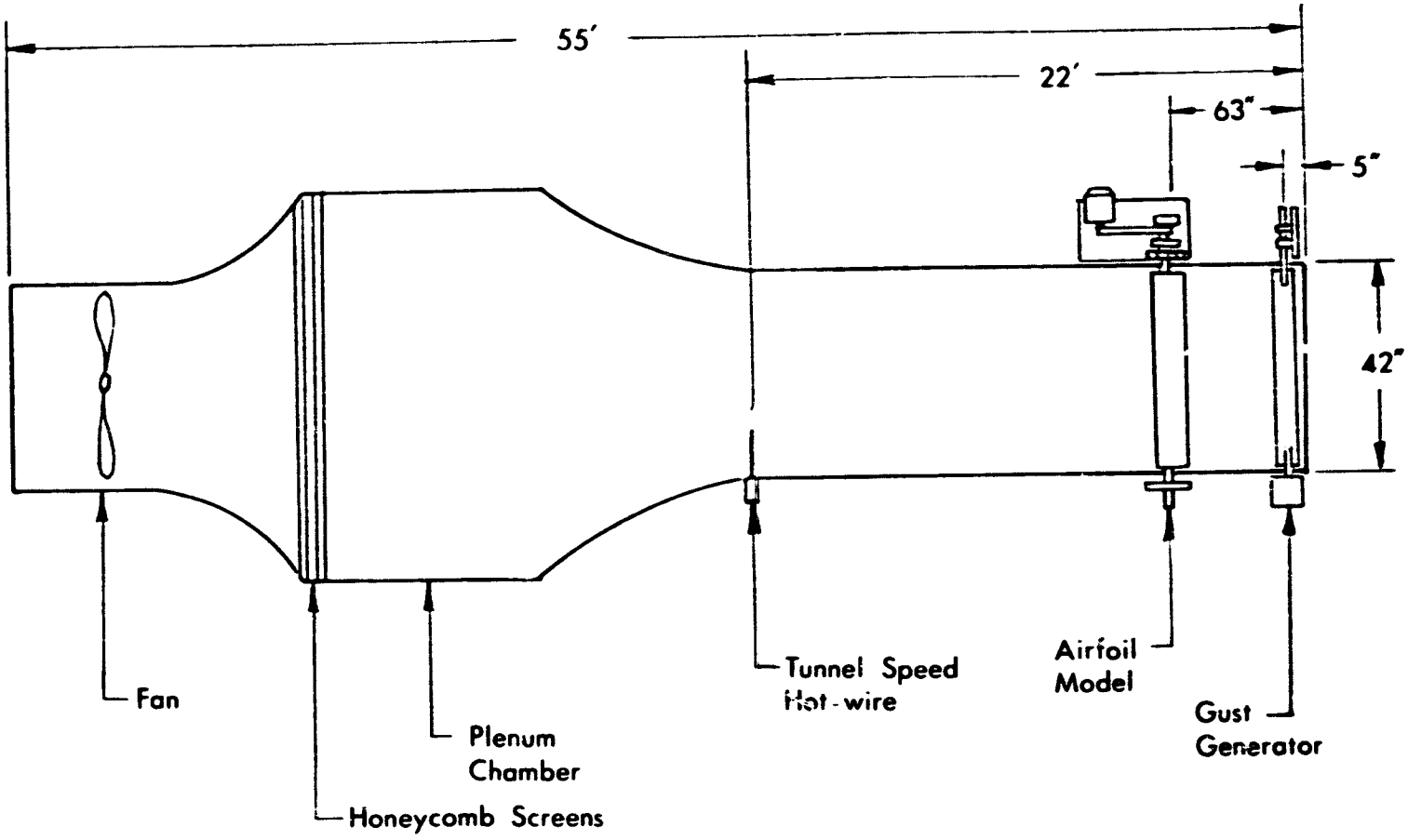

Figure 1. Low Turbulence Wind Tunnel

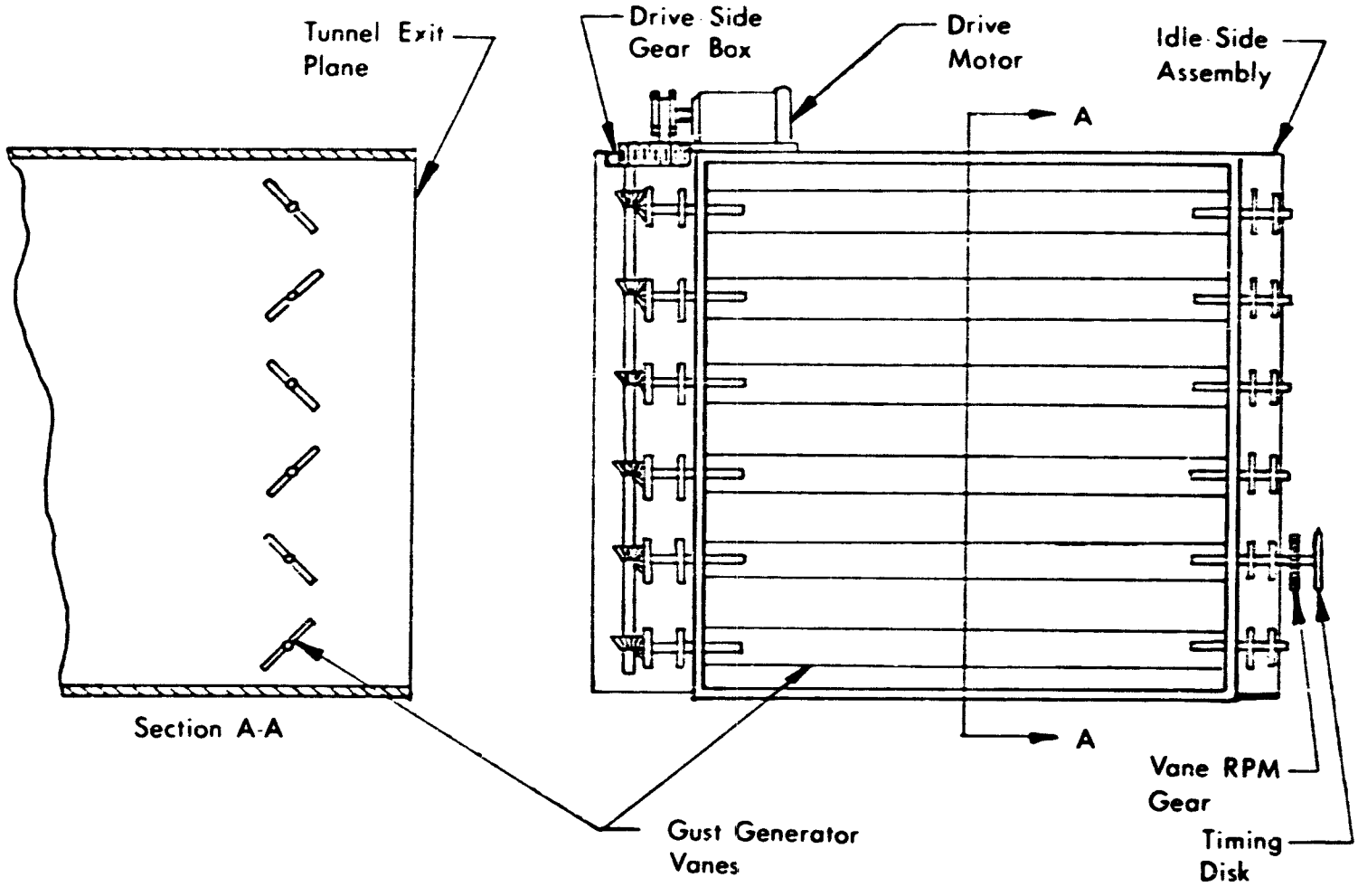

Figure 2. Gust Generator Mechanism

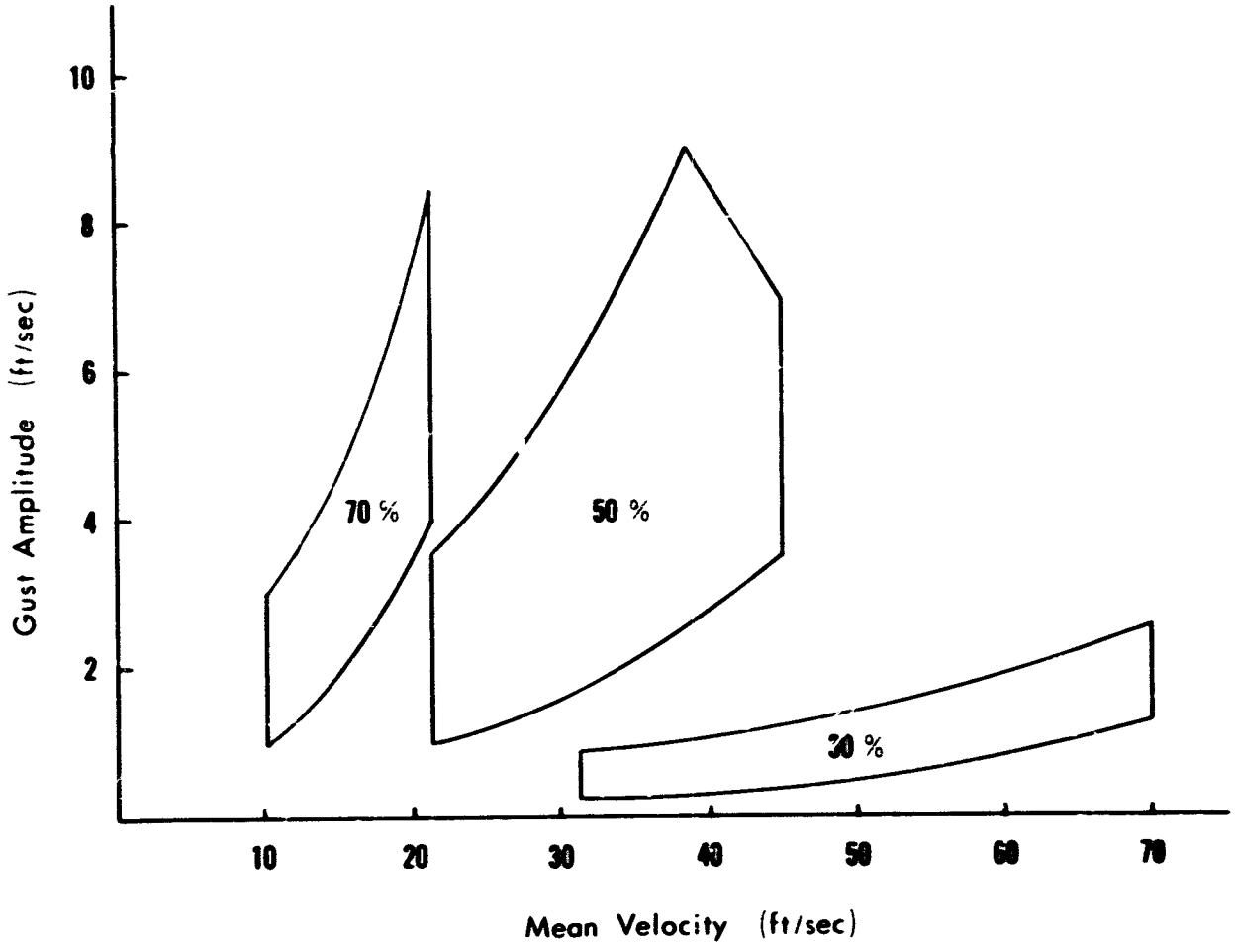

Figure 3. Gust Generator Operational Limits (0.67 - 2 Hz)

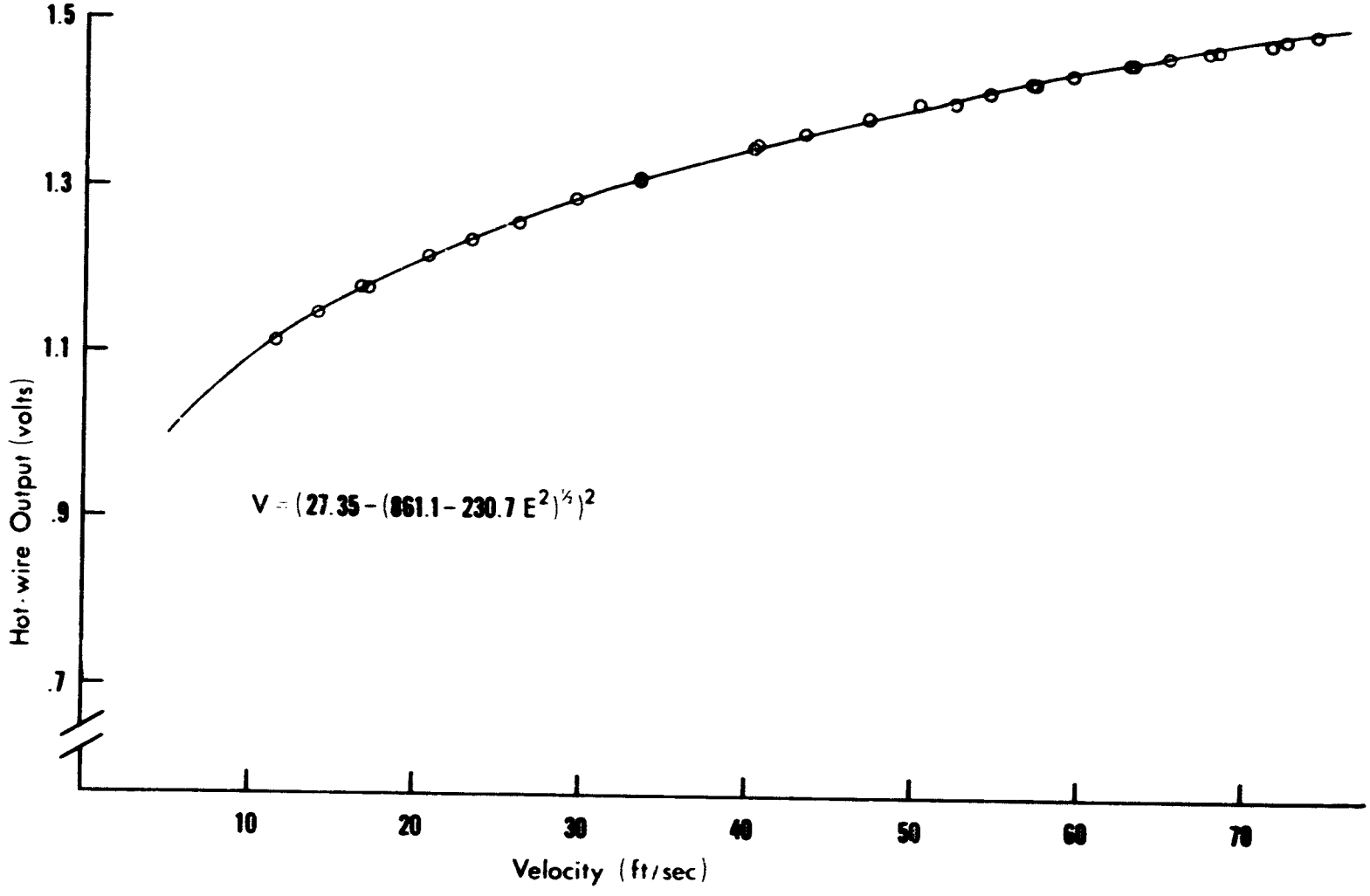

Figure 4. Hot-wire Calibration Curve

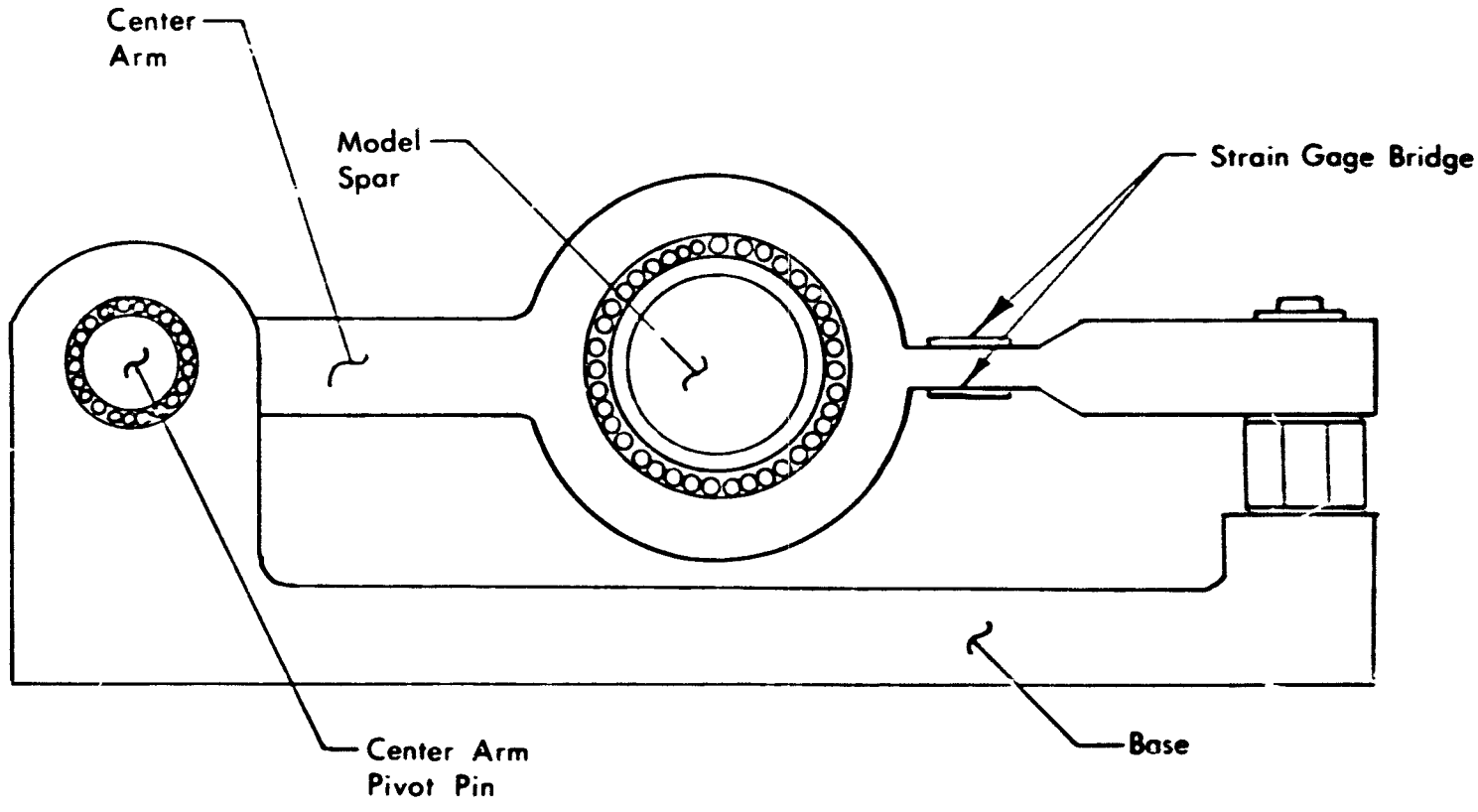

Figure 5. Main Bearing Assembly

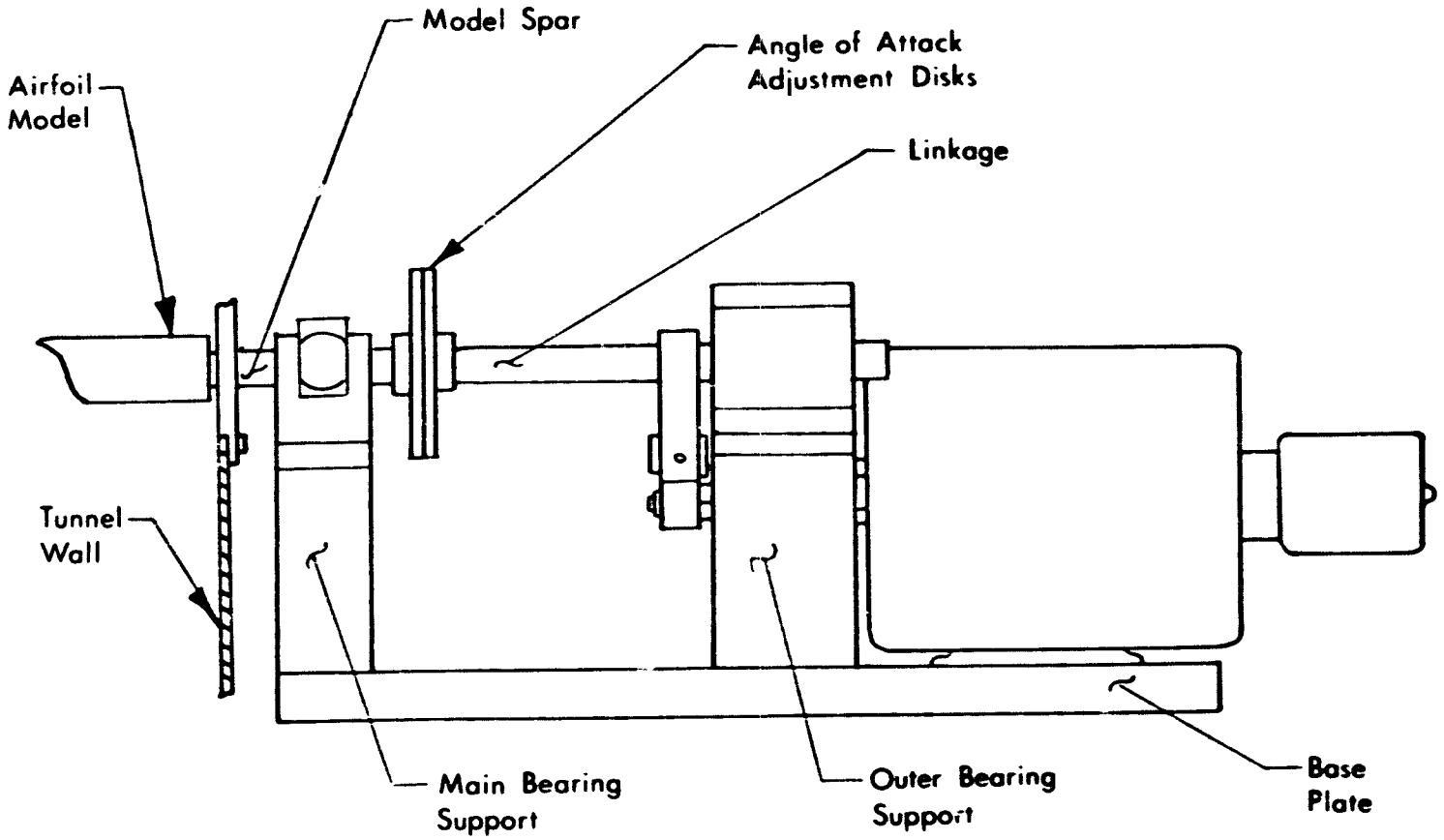

Figure 6. Airfoil Oscillating Mechanism (Front View)

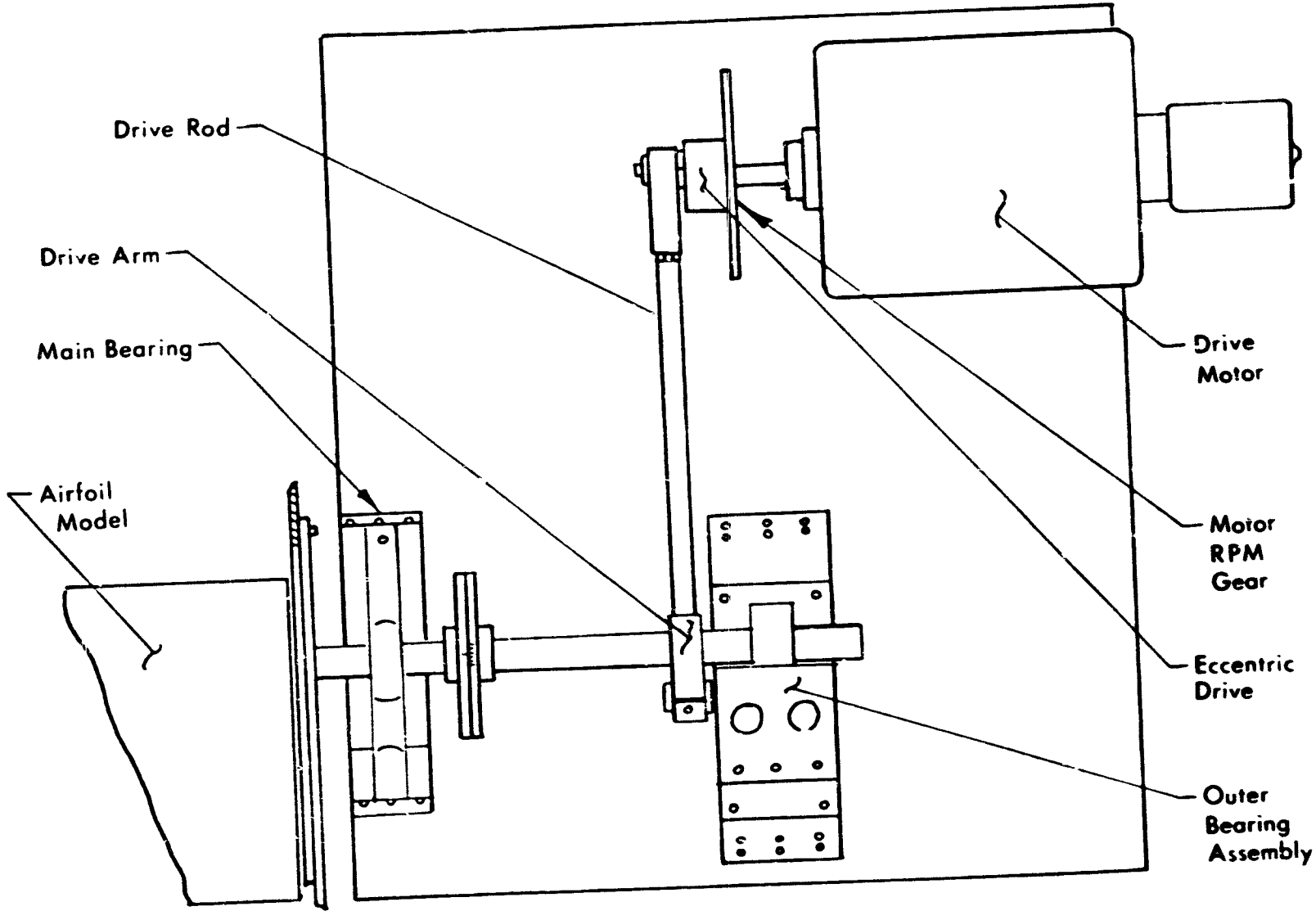

Figure 7. Airfoil Oscillating Mechanism (Top View)

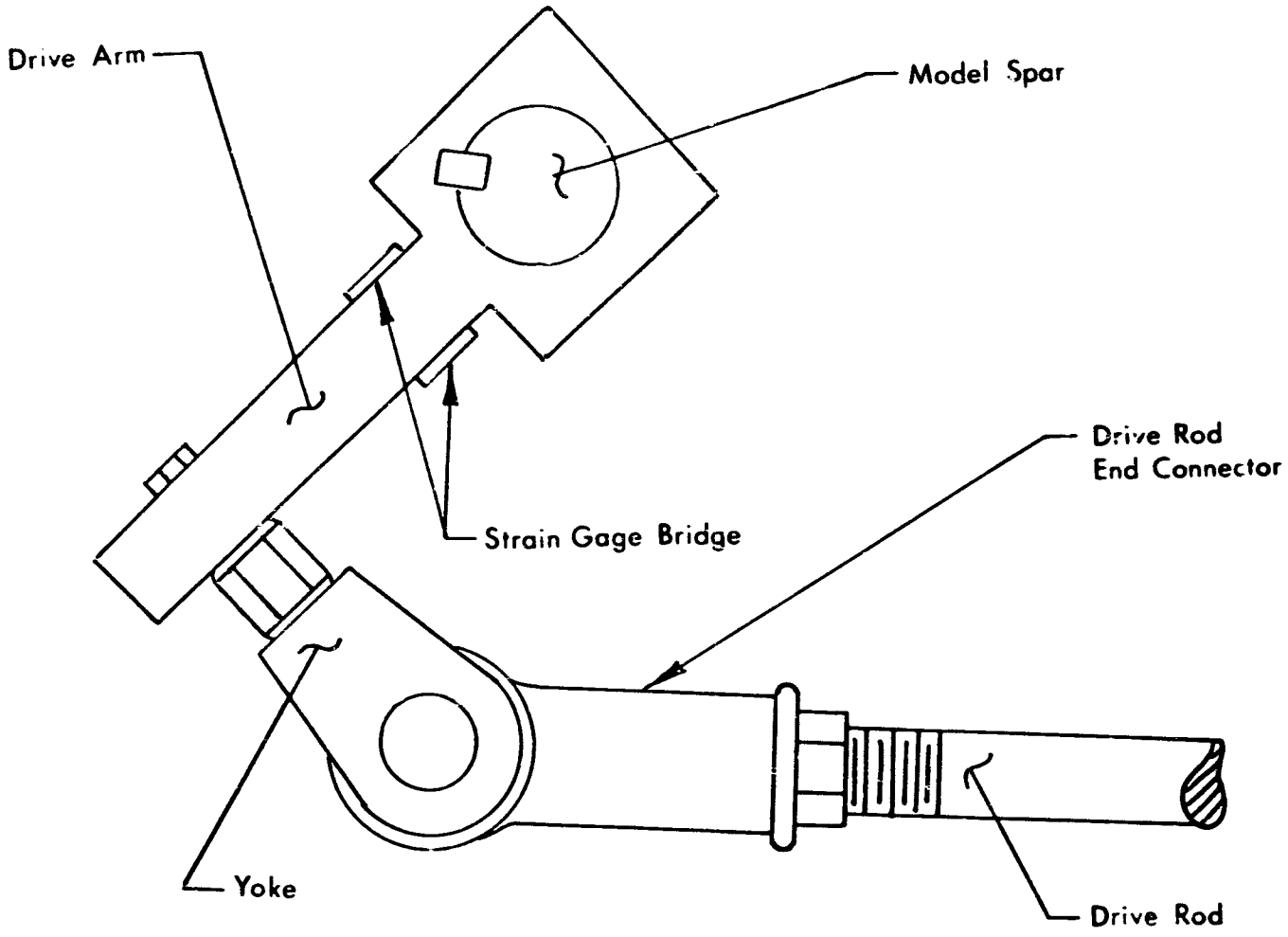

Figure 8. Drive Arm and Drive Rod Assembly

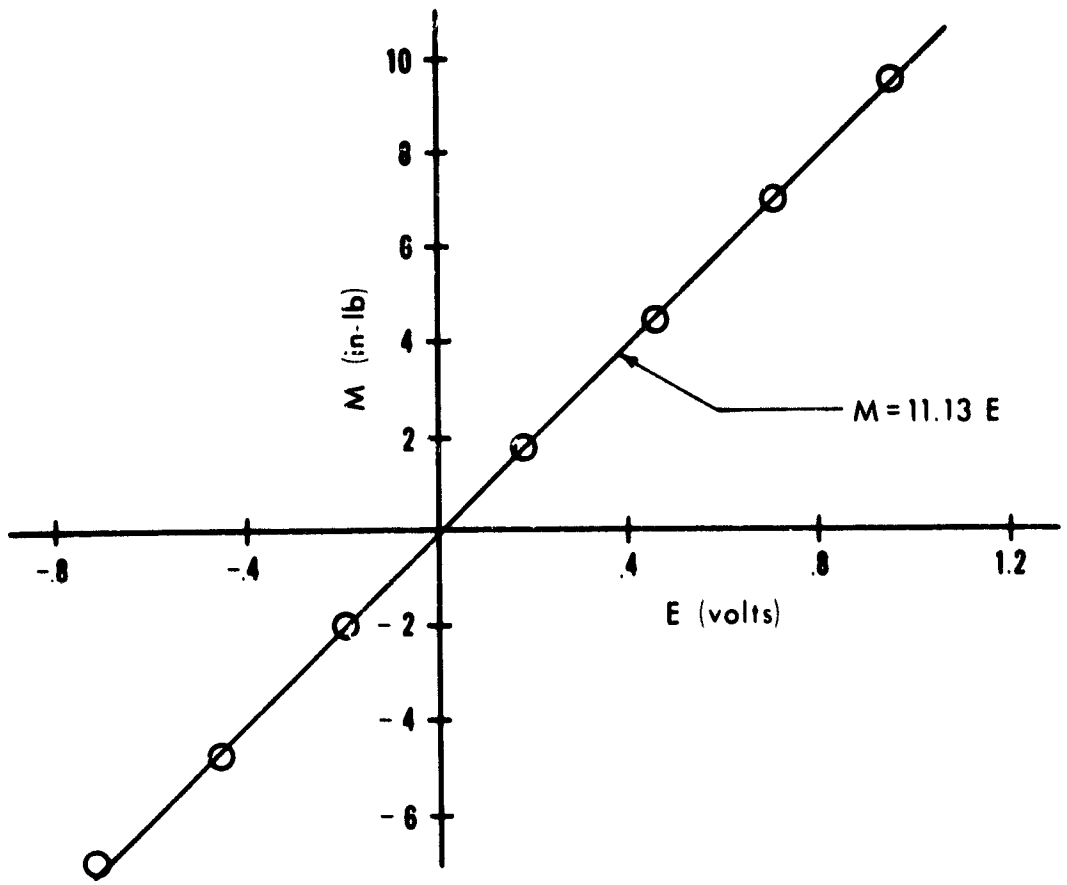

Figure 9. Moment Calibration Curve

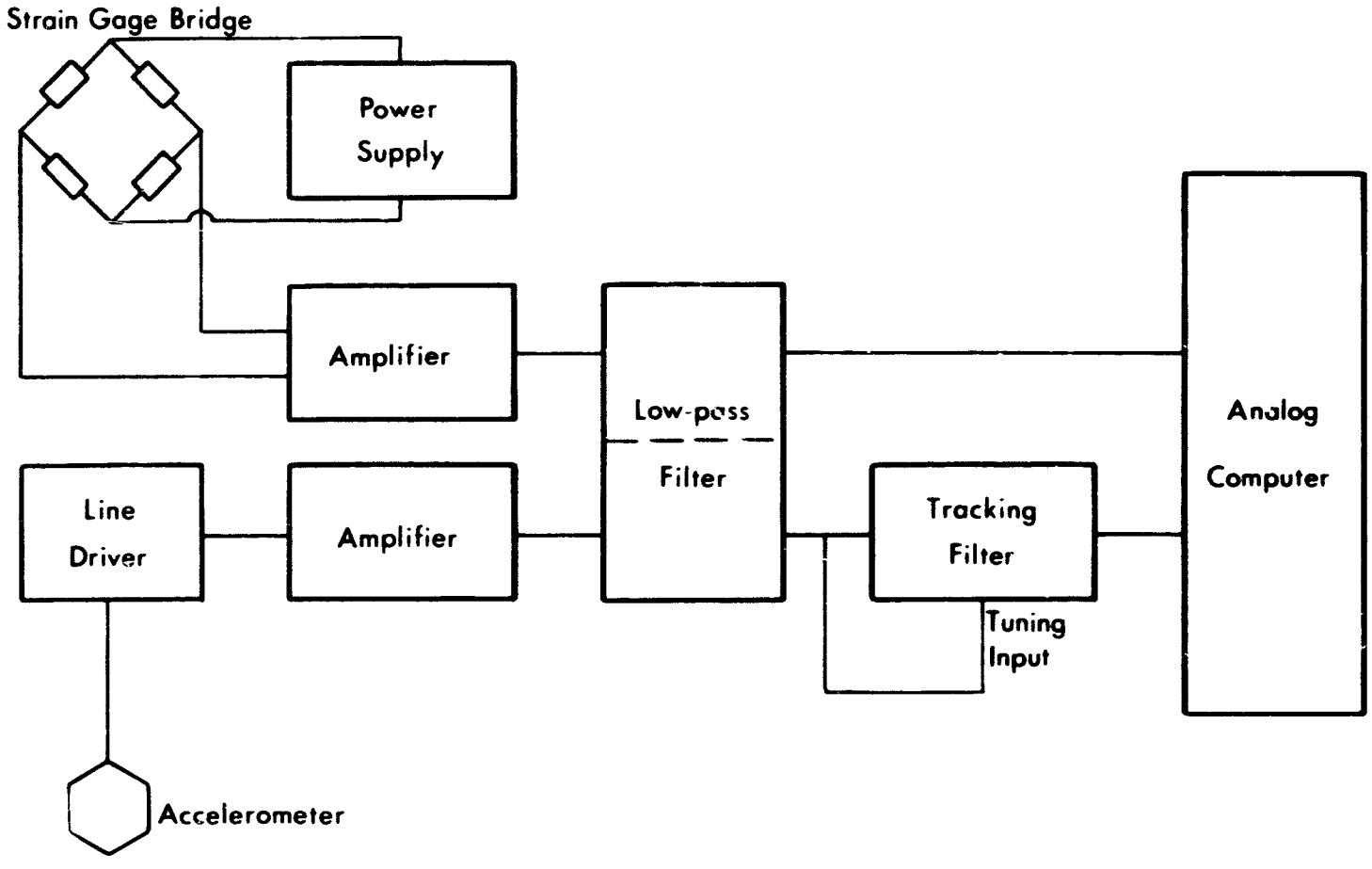

Figure 10. Electronic Data Acquisition Equipment

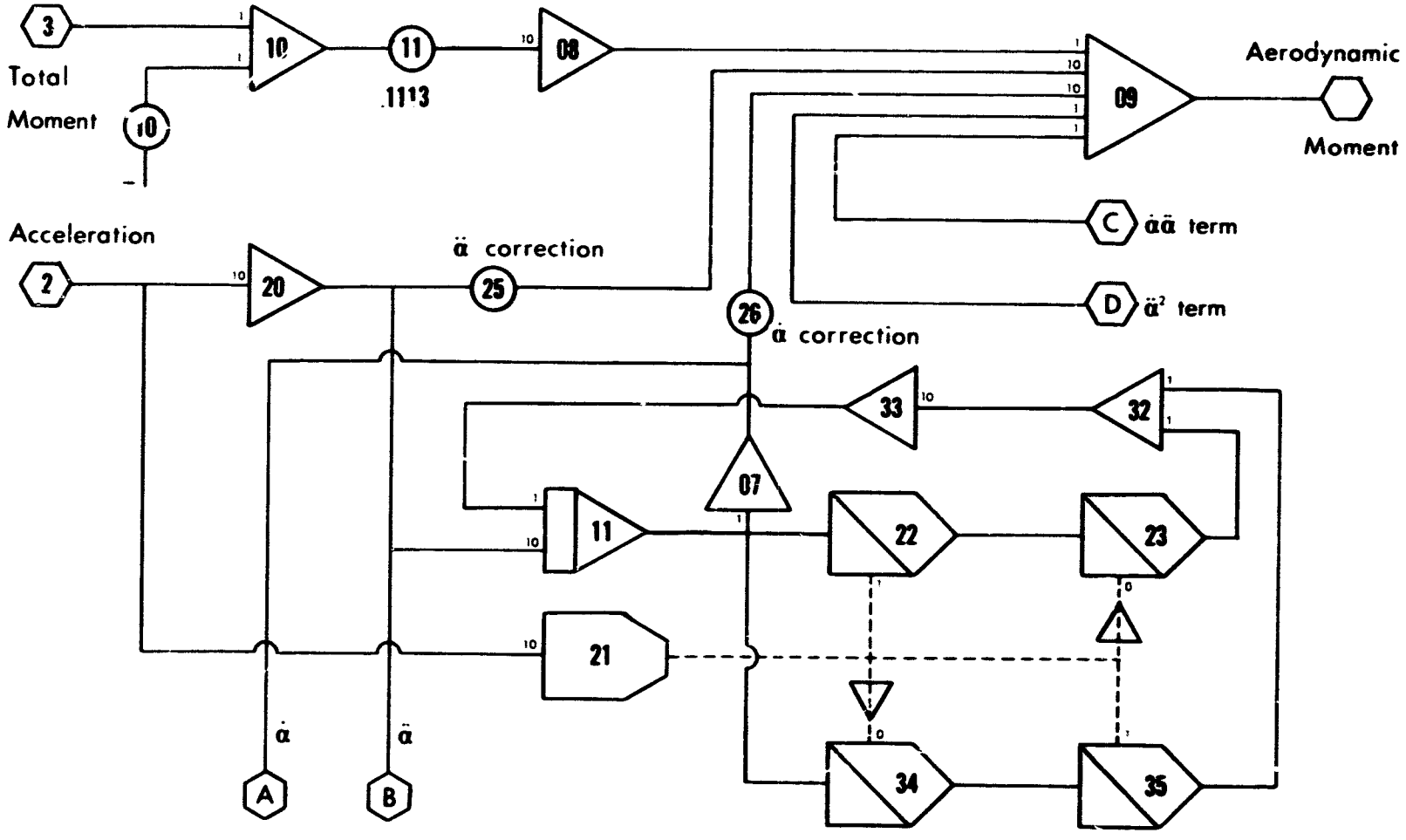

Figure 11. Moment Correction Circuit (α̈, α̇)

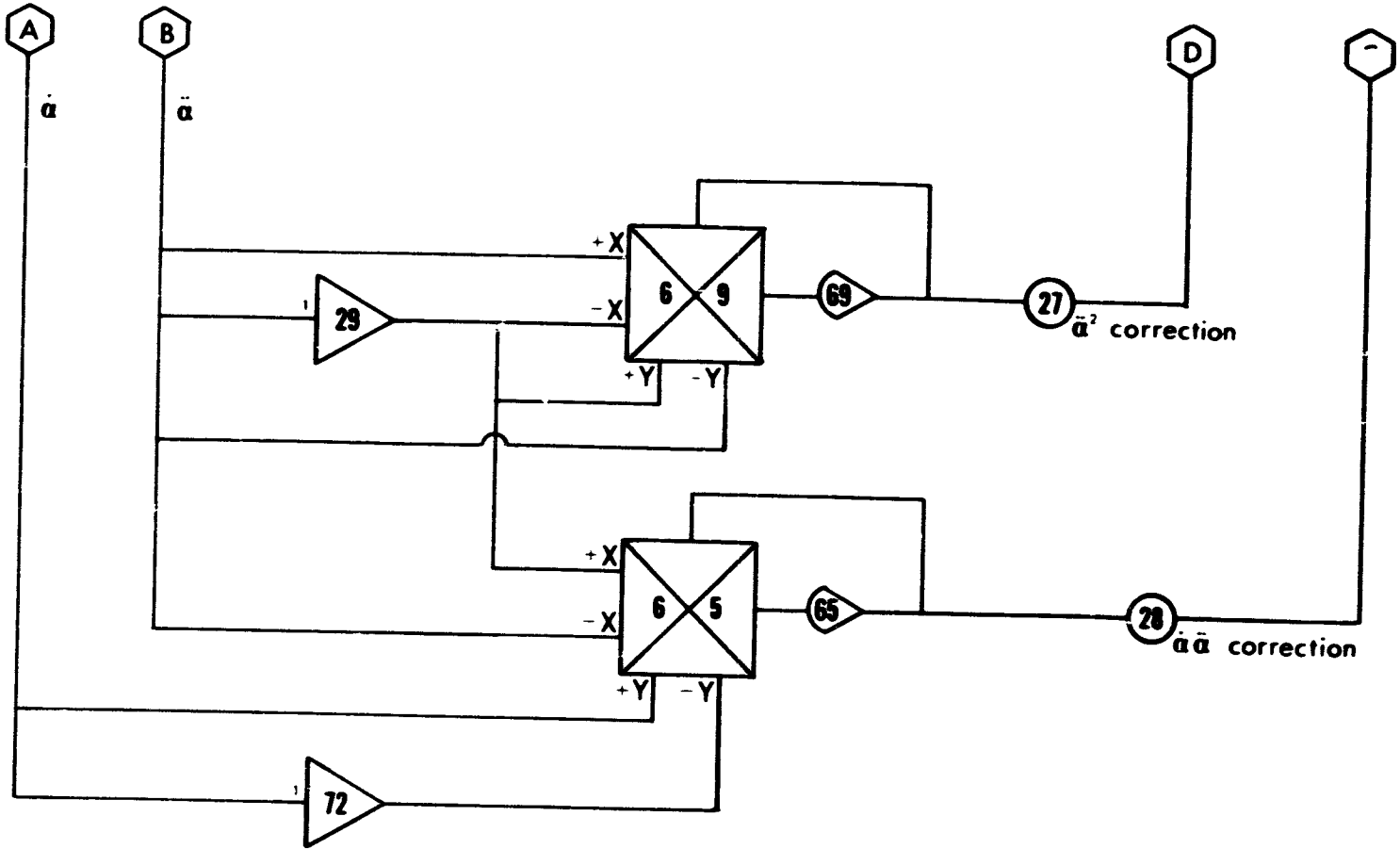

Figure 12. Moment Correction Circuit ($\ddot{\alpha}^2$, $\delta\ddot{\alpha}$)

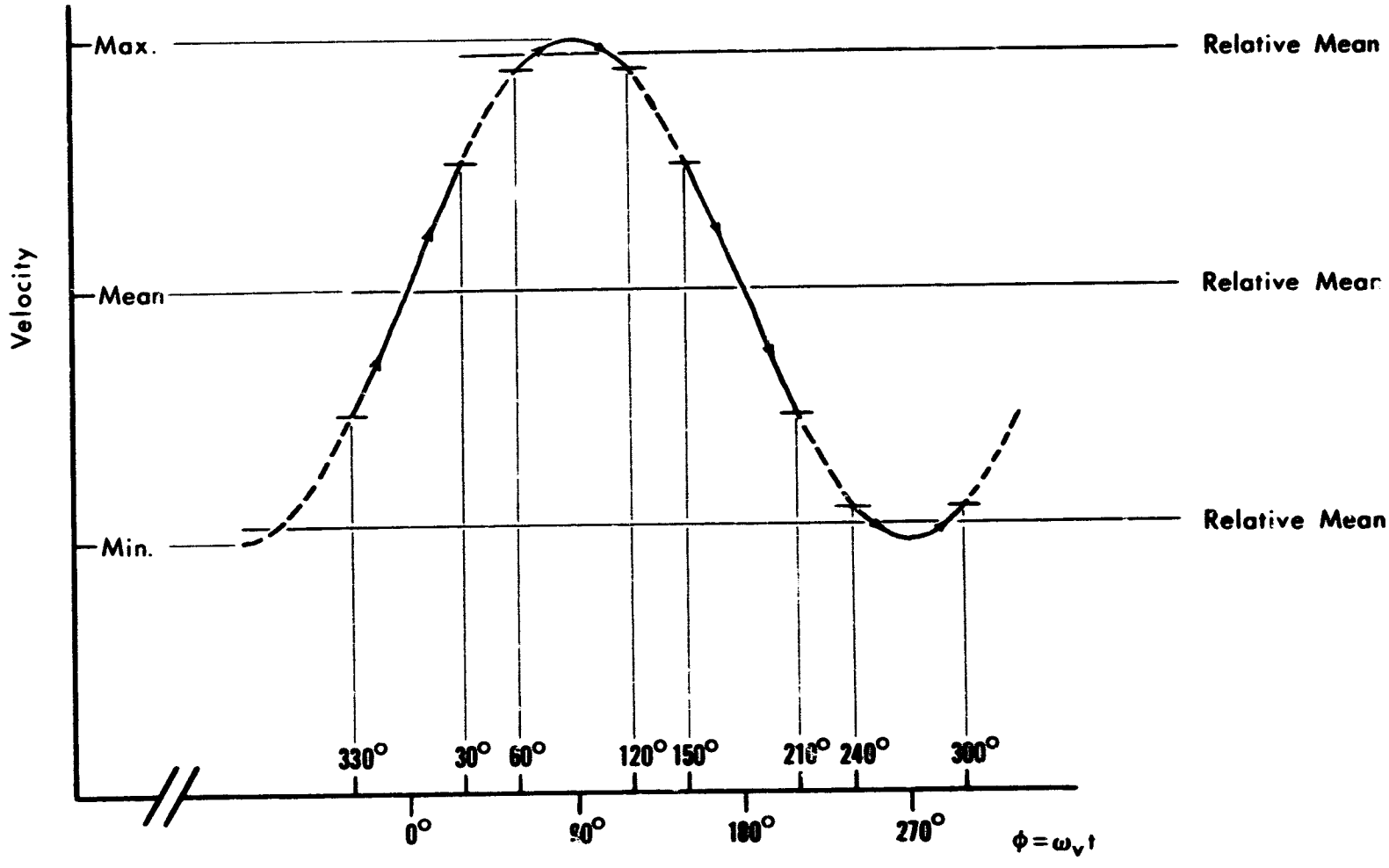

Figure 13. Gust Generator Velocity Curve (R=6)

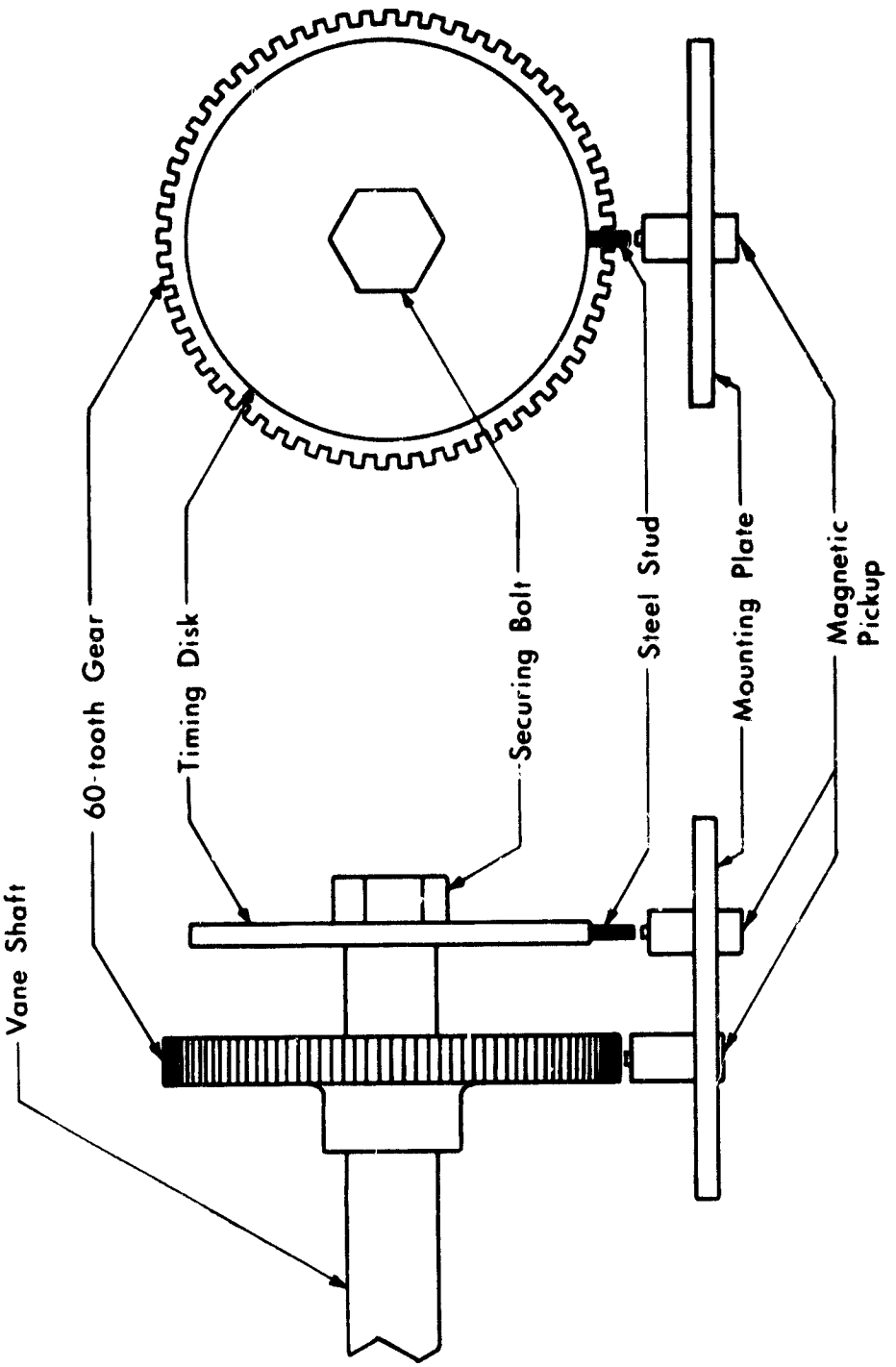

Figure 14. Timing Disk Assembly

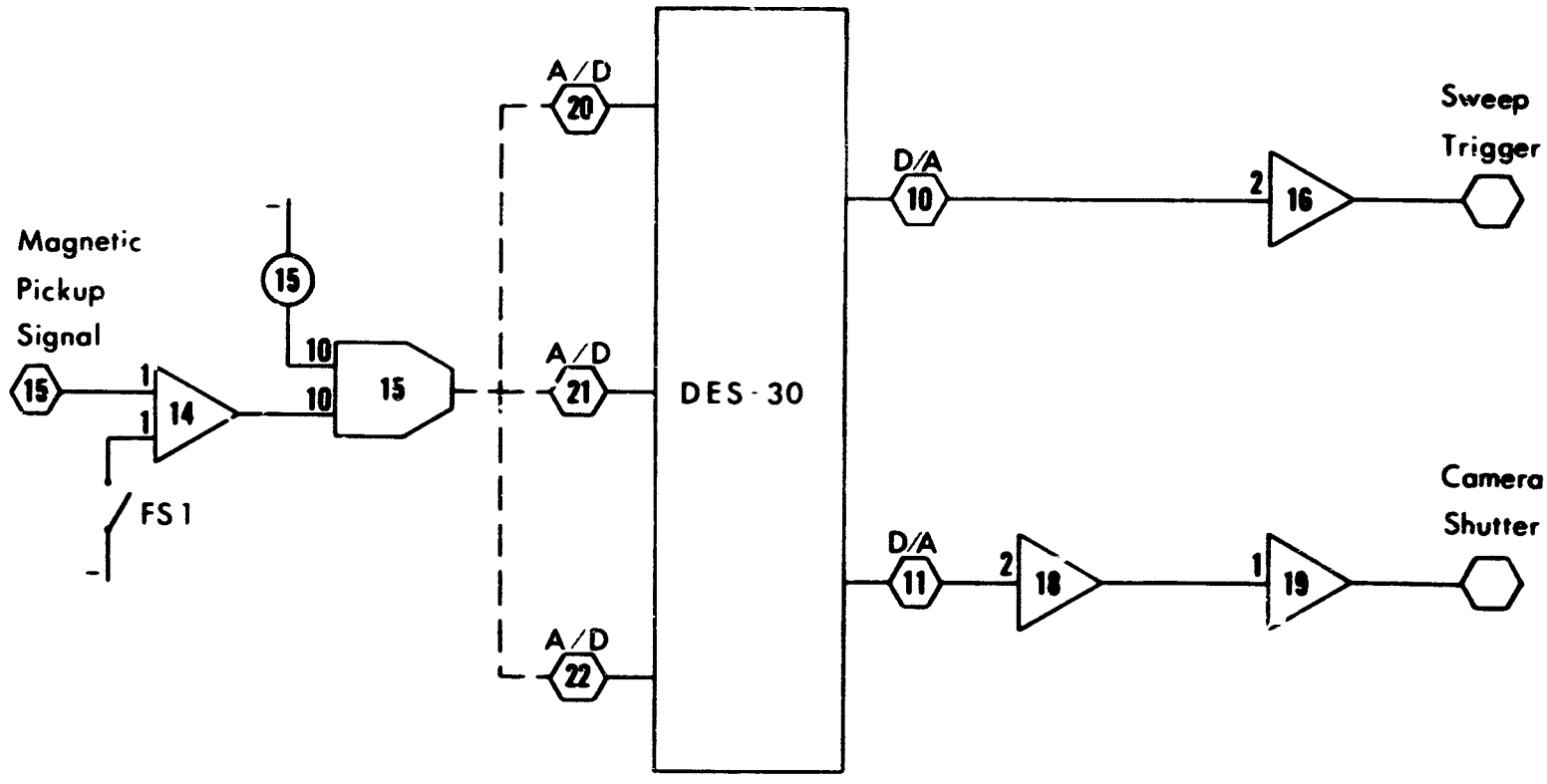

Figure 15. Analog Shutter Synchronization Circuit

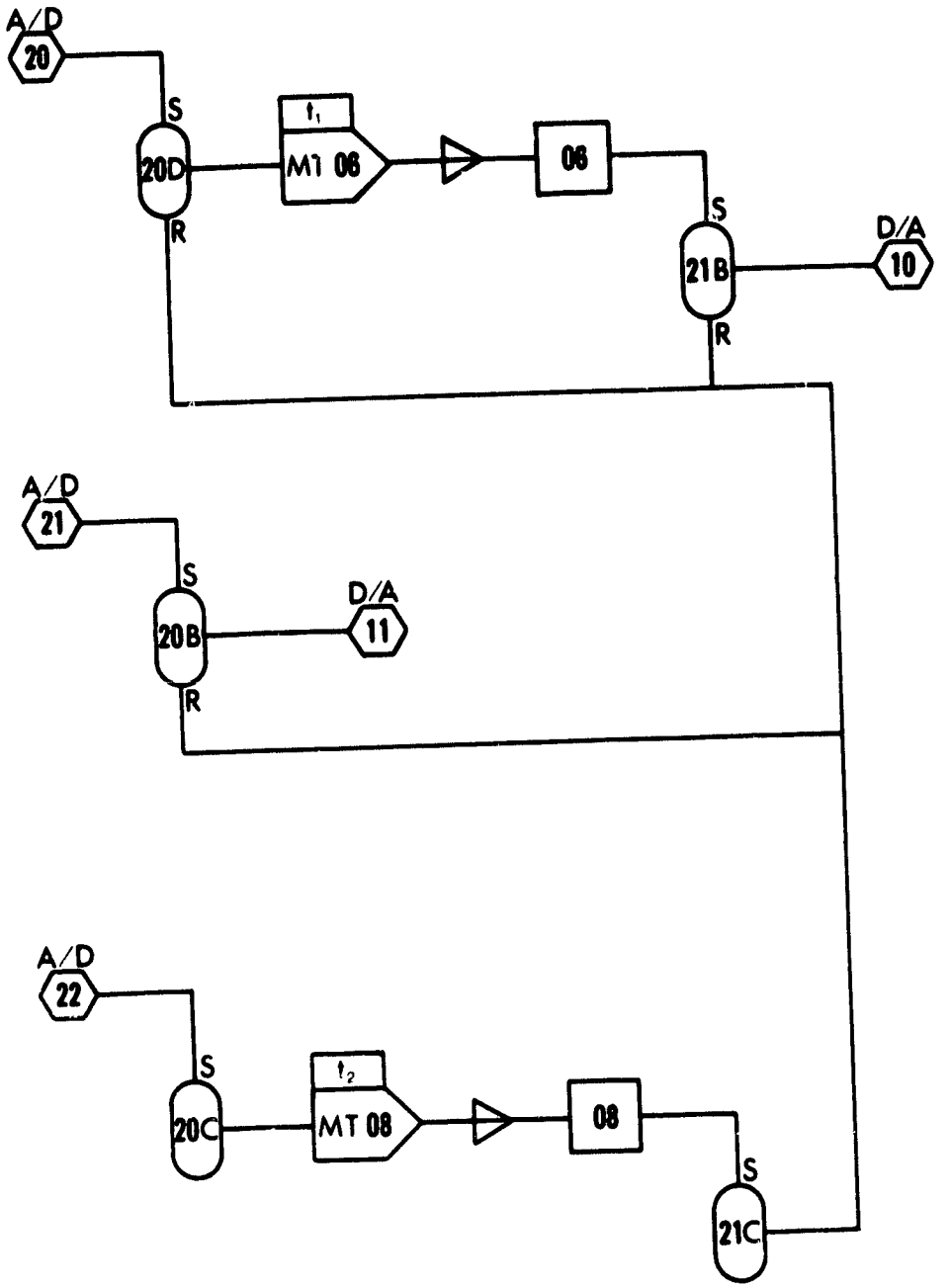

Figure 16. Digital Shutter Synchronization Circuit

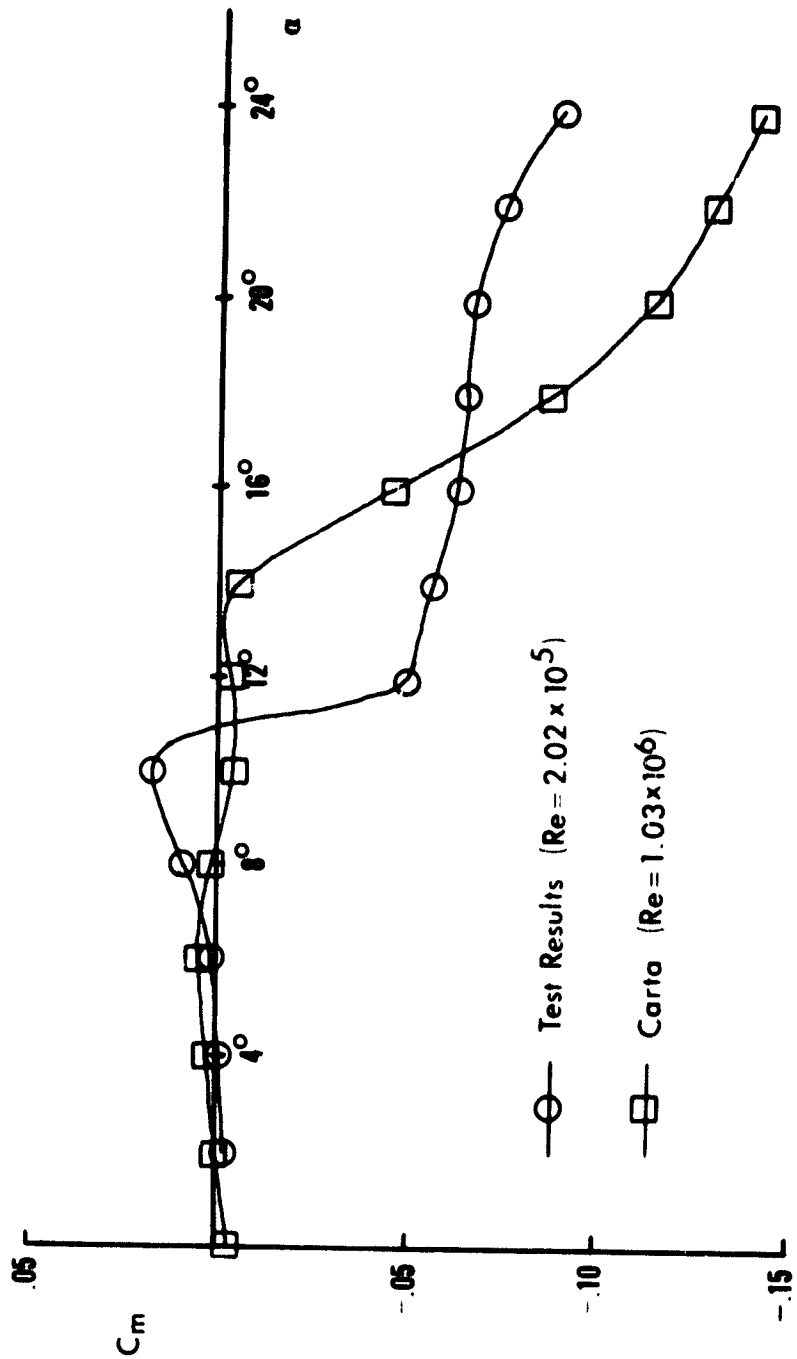

Figure 17. Static Moment Curves

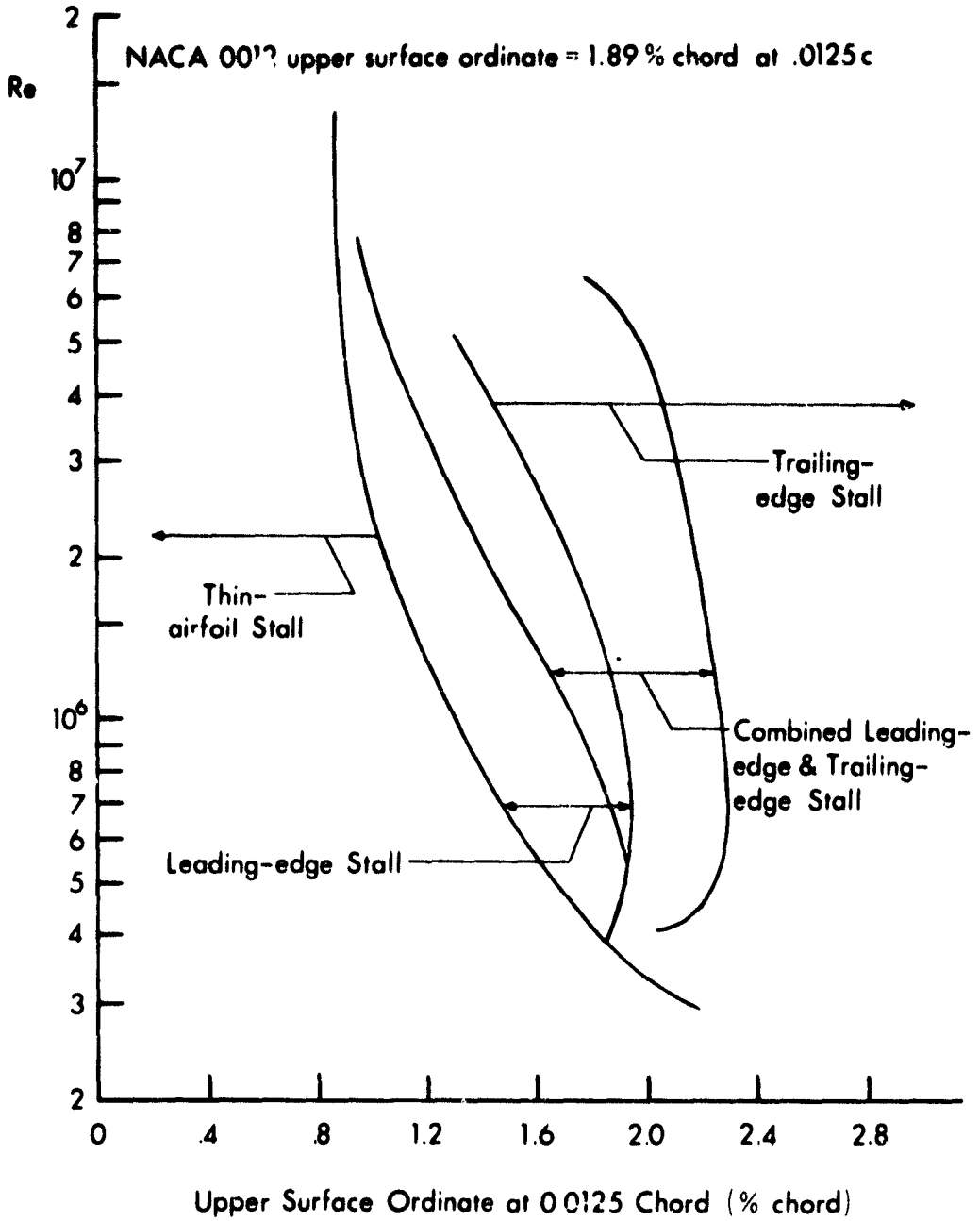

Figure 18. Static Stall Type as a Function of Reynolds Number and Leading Edge Curvature (Reference 23)

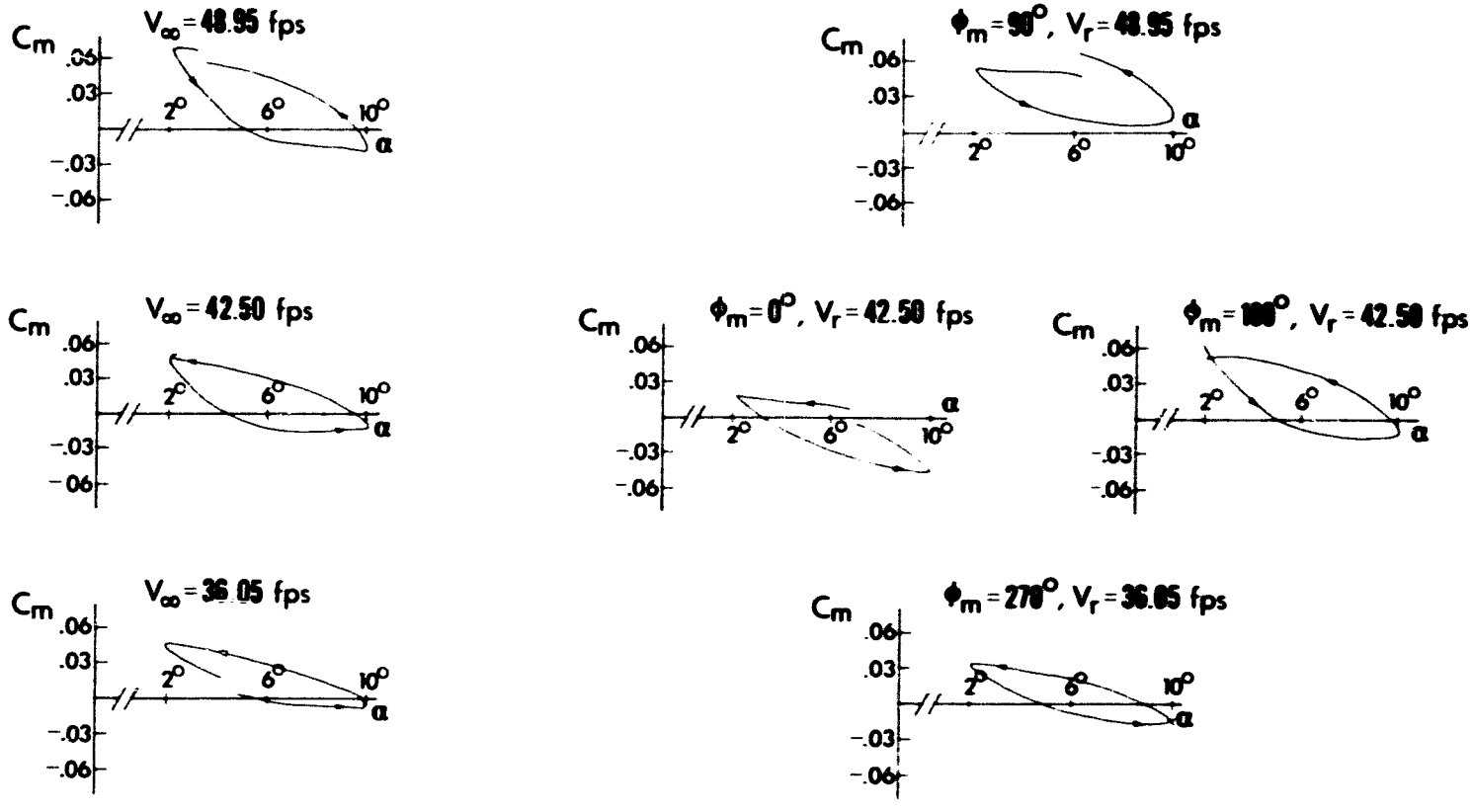

Figure 19. Sequential C_m vs. α for Oscillations About 6° at 6 Hz in Constant and 1 Hz Varying Freestreams

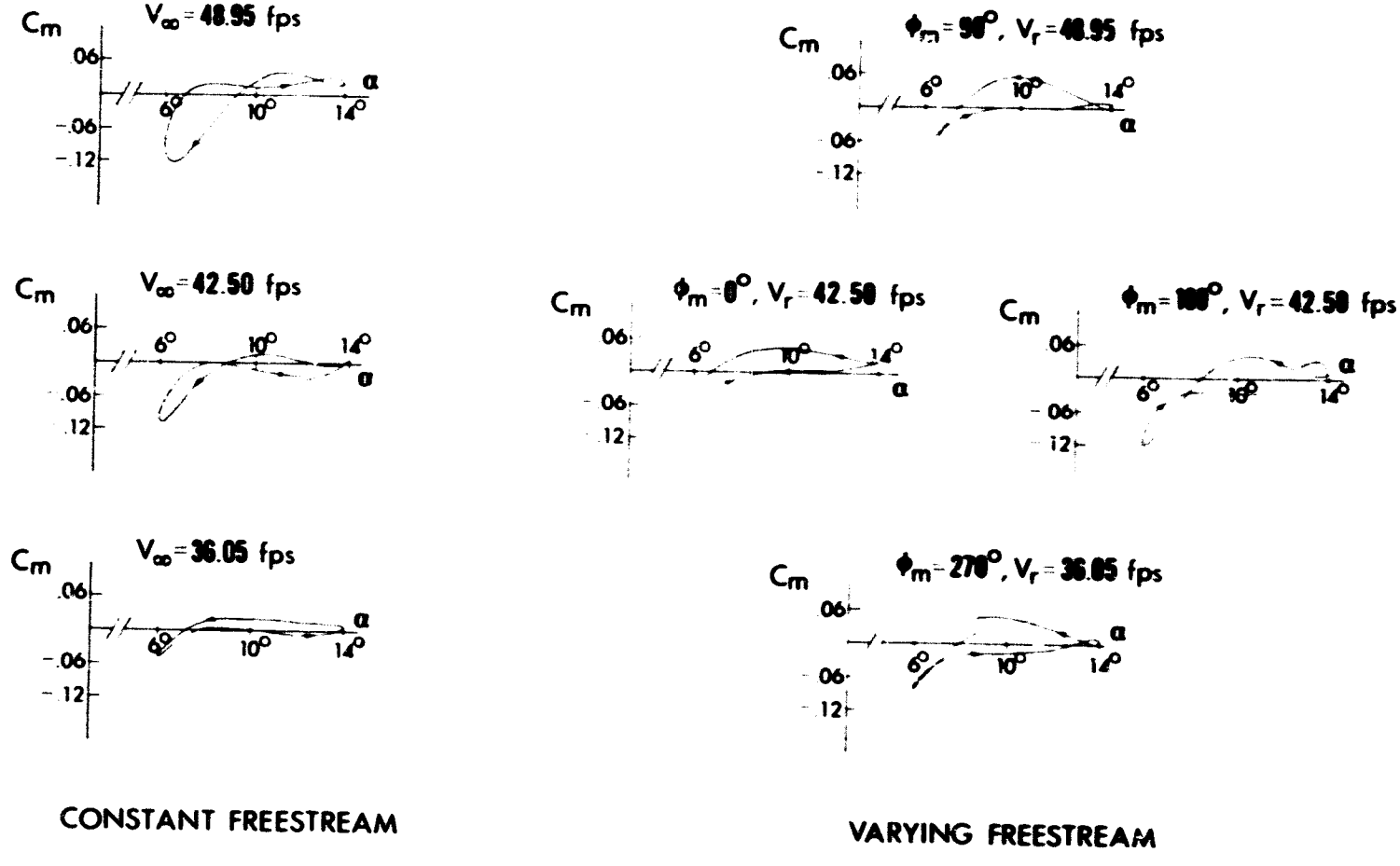

Figure 20. Sequential C_m vs. α for Oscillations About 10° at 6 Hz in Constant and 1 Hz Varying Freestreams

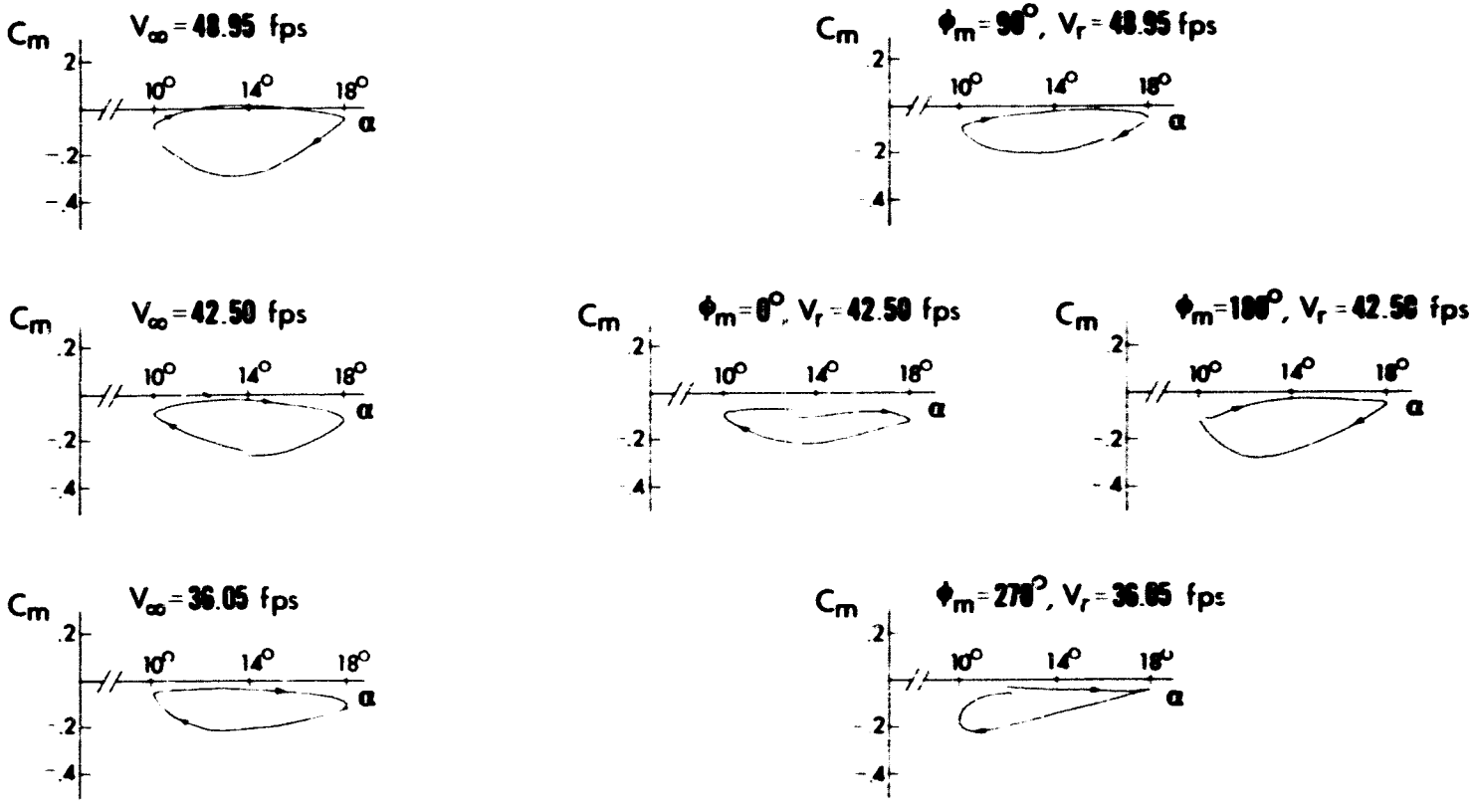

Figure 21. Sequential C_m vs. α for Oscillations About 14° at 6 Hz in Constant and 1 Hz Varying Freestreams

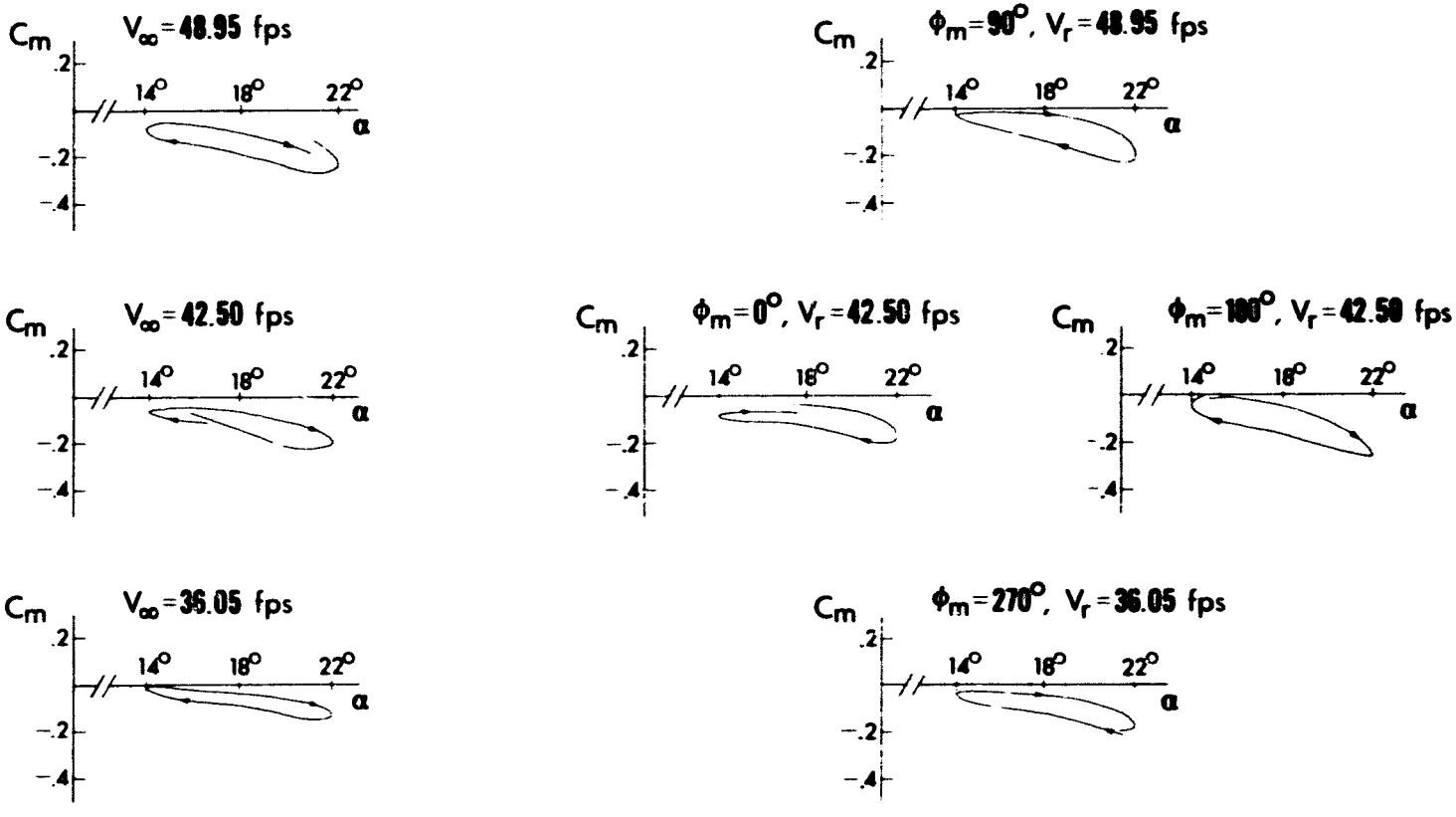

Figure 22. Sequential C_m vs. α for Oscillations About 18° at 6 Hz in Constant and 1 Hz Varying Freestreams

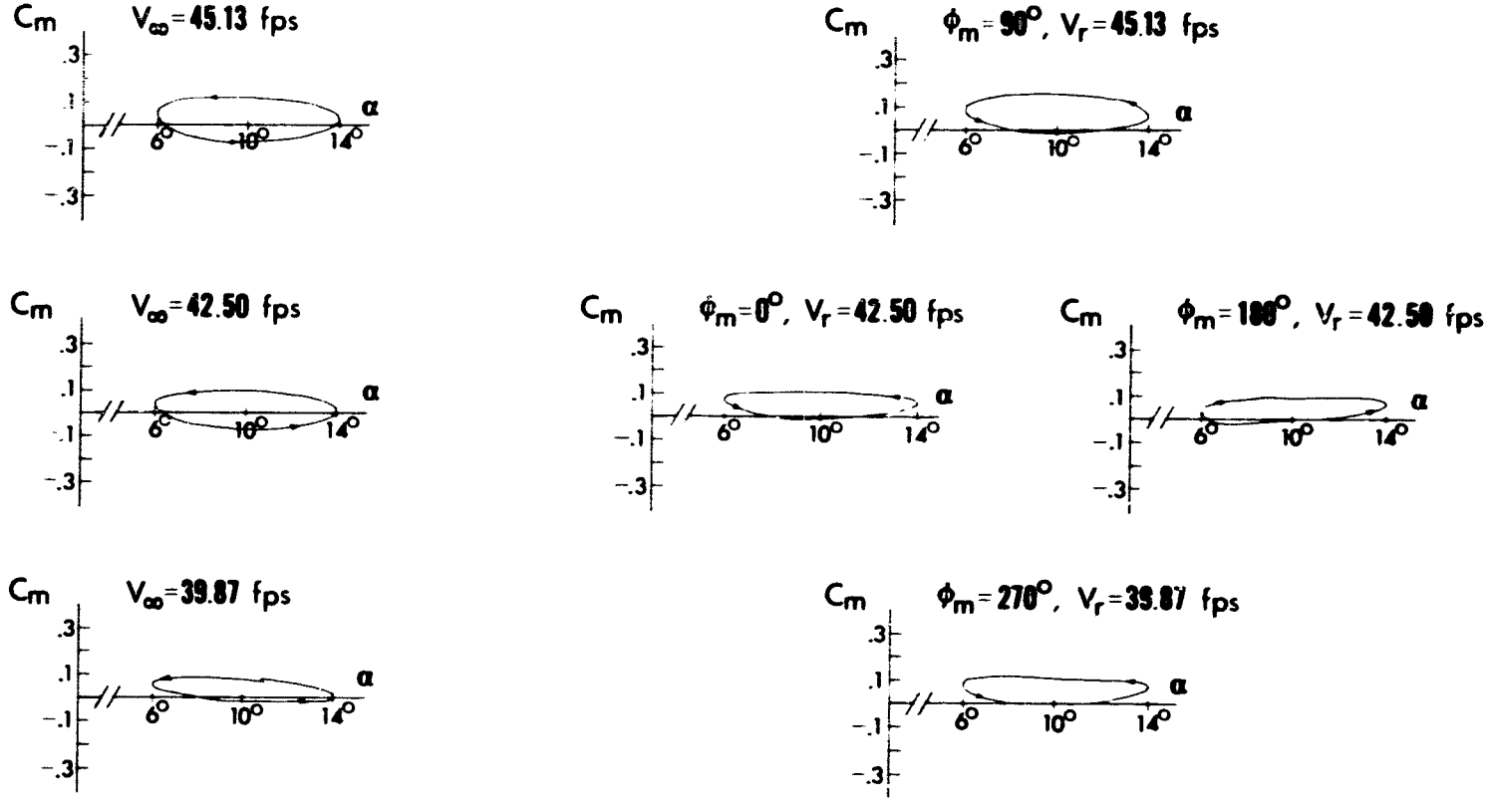

Figure 23. Sequential C_m vs. α for Oscillations About 10° at 12 Hz in Constant and 2 Hz Varying Freestreams

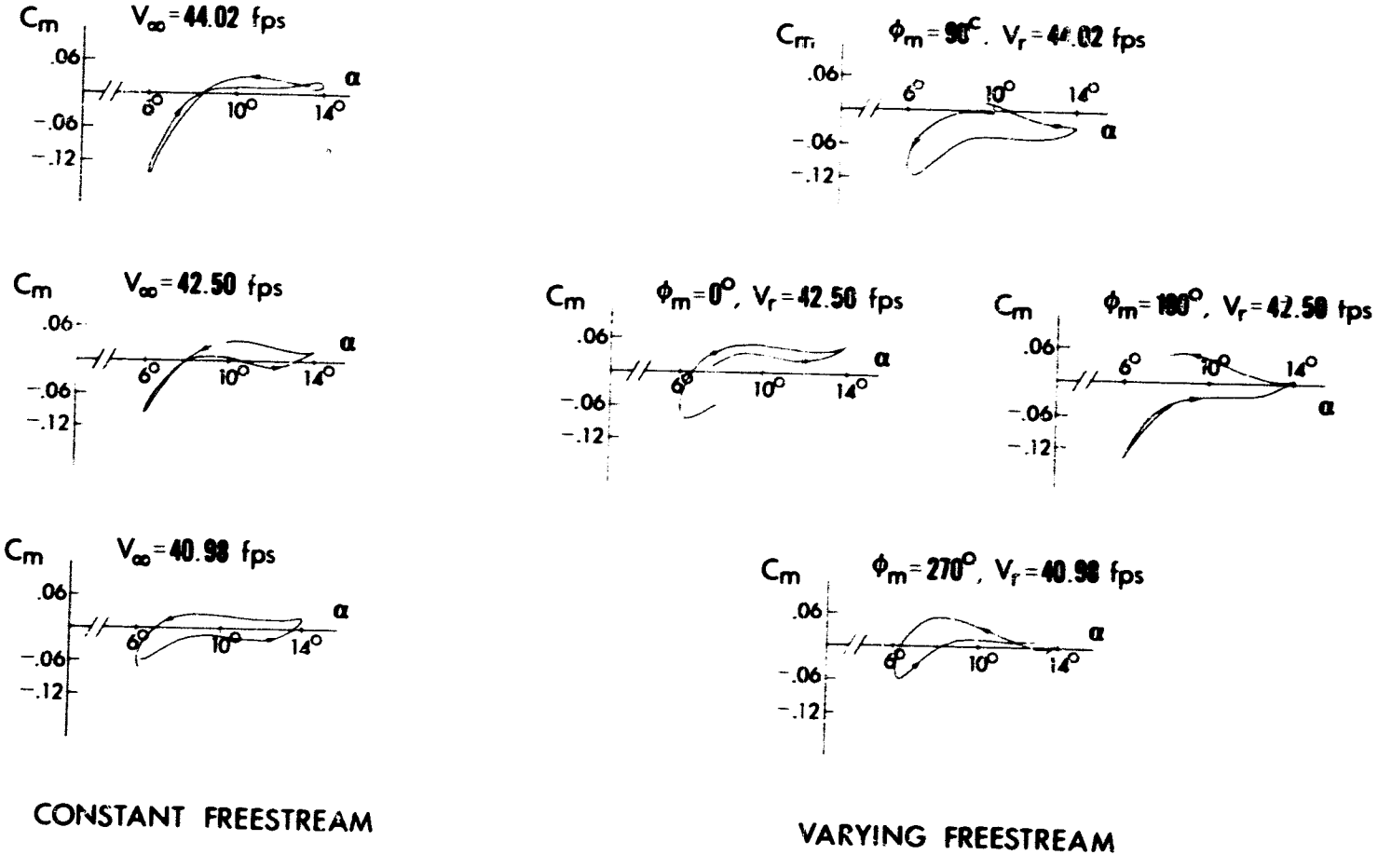

Figure 24. Sequential C_m vs. α for Oscillations About 10° at 6 Hz in Constant and 2 Hz Varying Freestreams

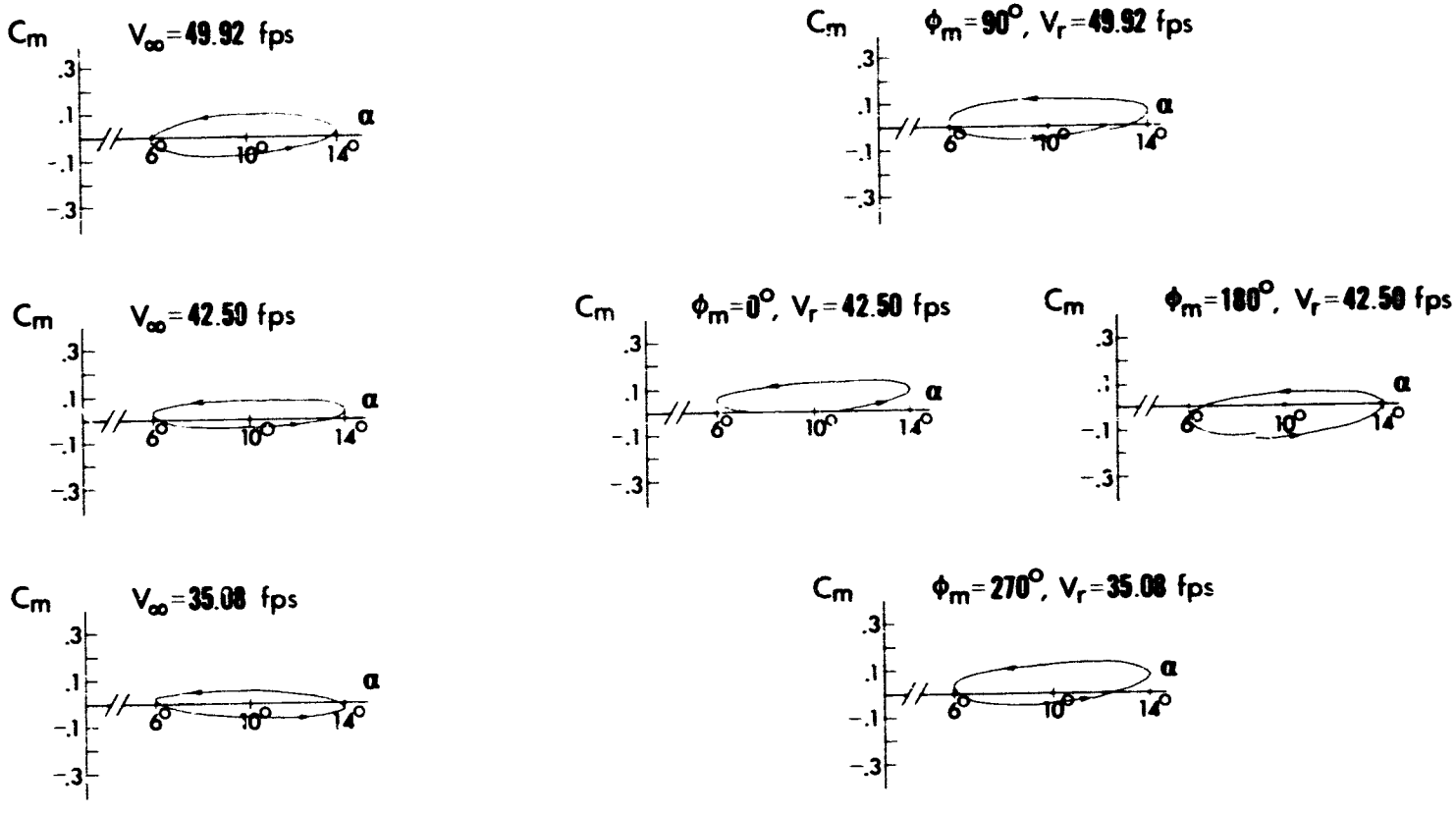

Figure 25. Sequential C_m vs. α for Oscillations About 10° at 12 Hz in Constant and 1 Hz Varying Freestreams

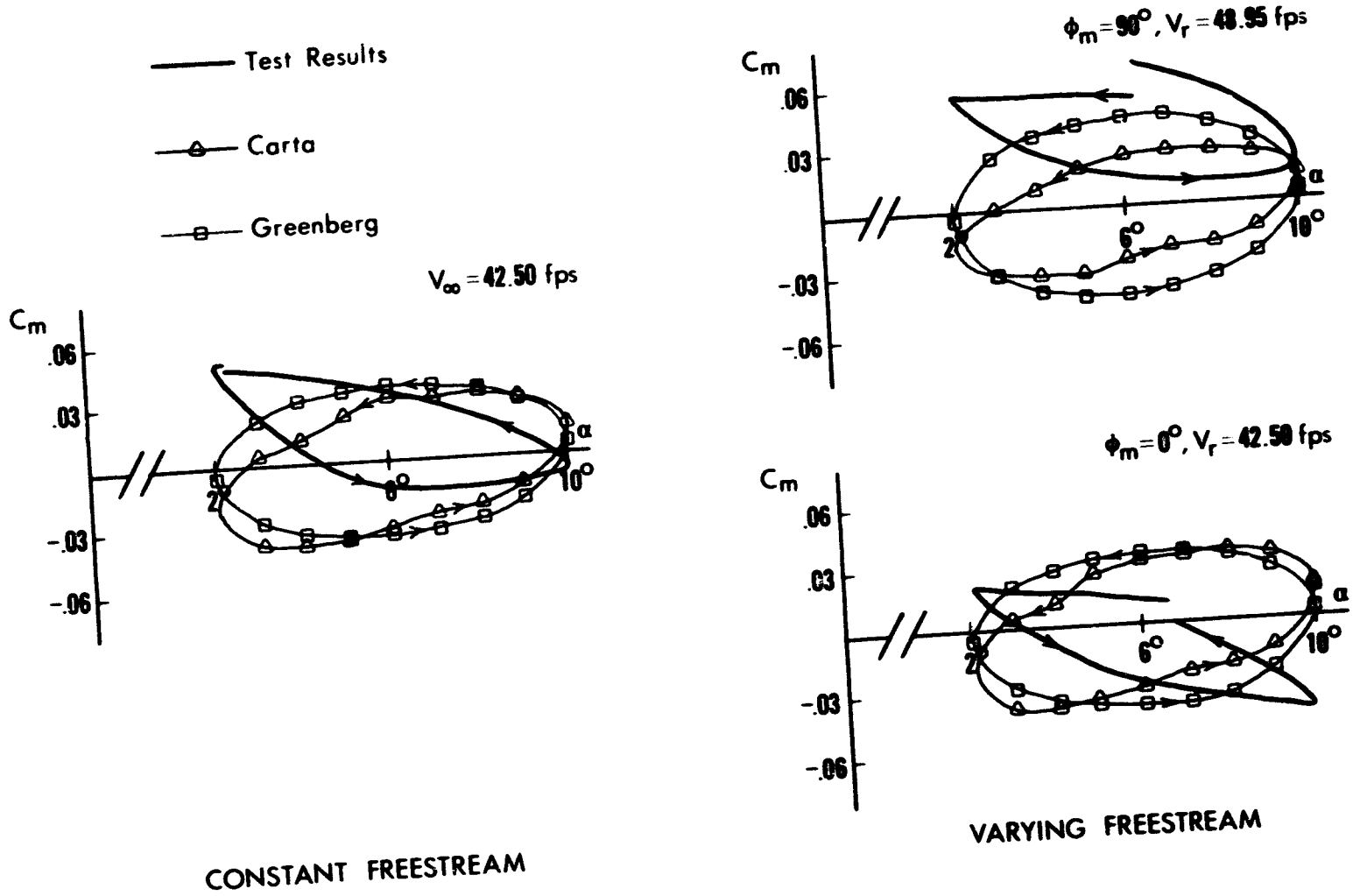

Figure 25. Analytical and Experimental C_m vs. α for Oscillations About 6° at 6 Hz in Constant and 1 Hz Varying Freestreams

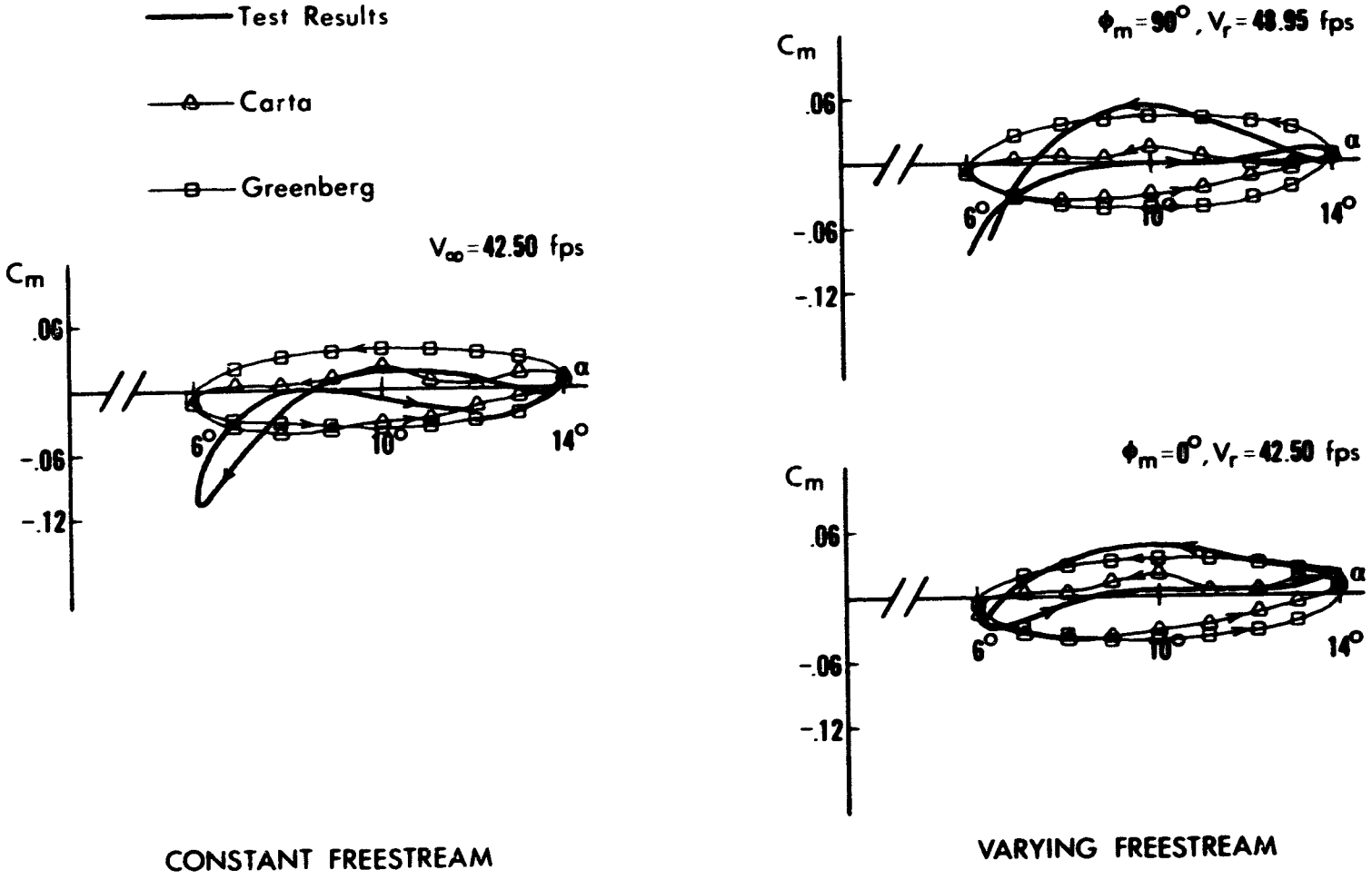

Figure 27. Analytical and Experimental C_m vs. α for Oscillations About 10° at 6 Hz in Constant and 1 Hz Varying Freestreams

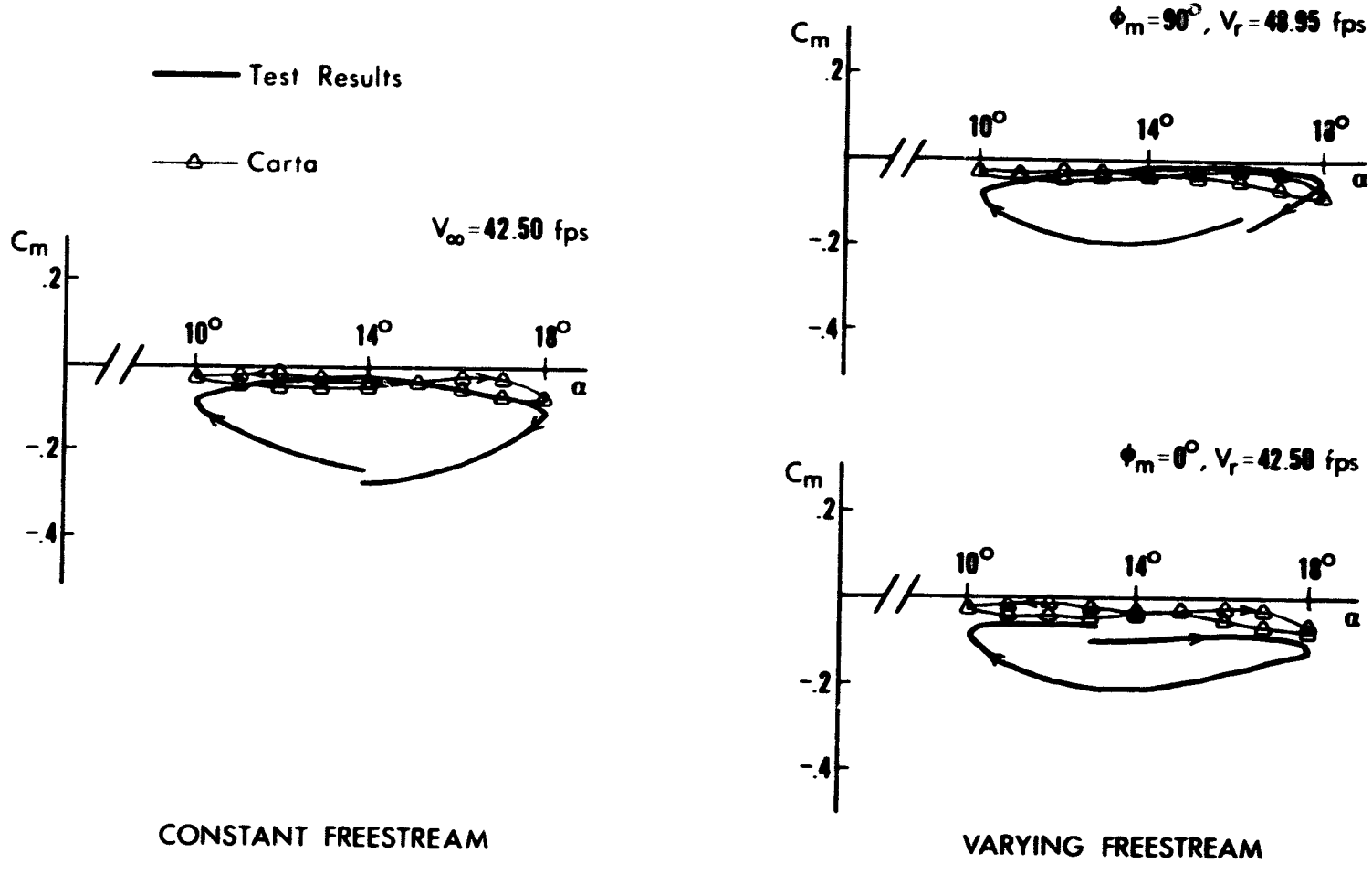

Figure 28. Analytical and Experimental C_m vs. α for Oscillations About 14° at 6 Hz in Constant and 1 Hz Varying Freestreams

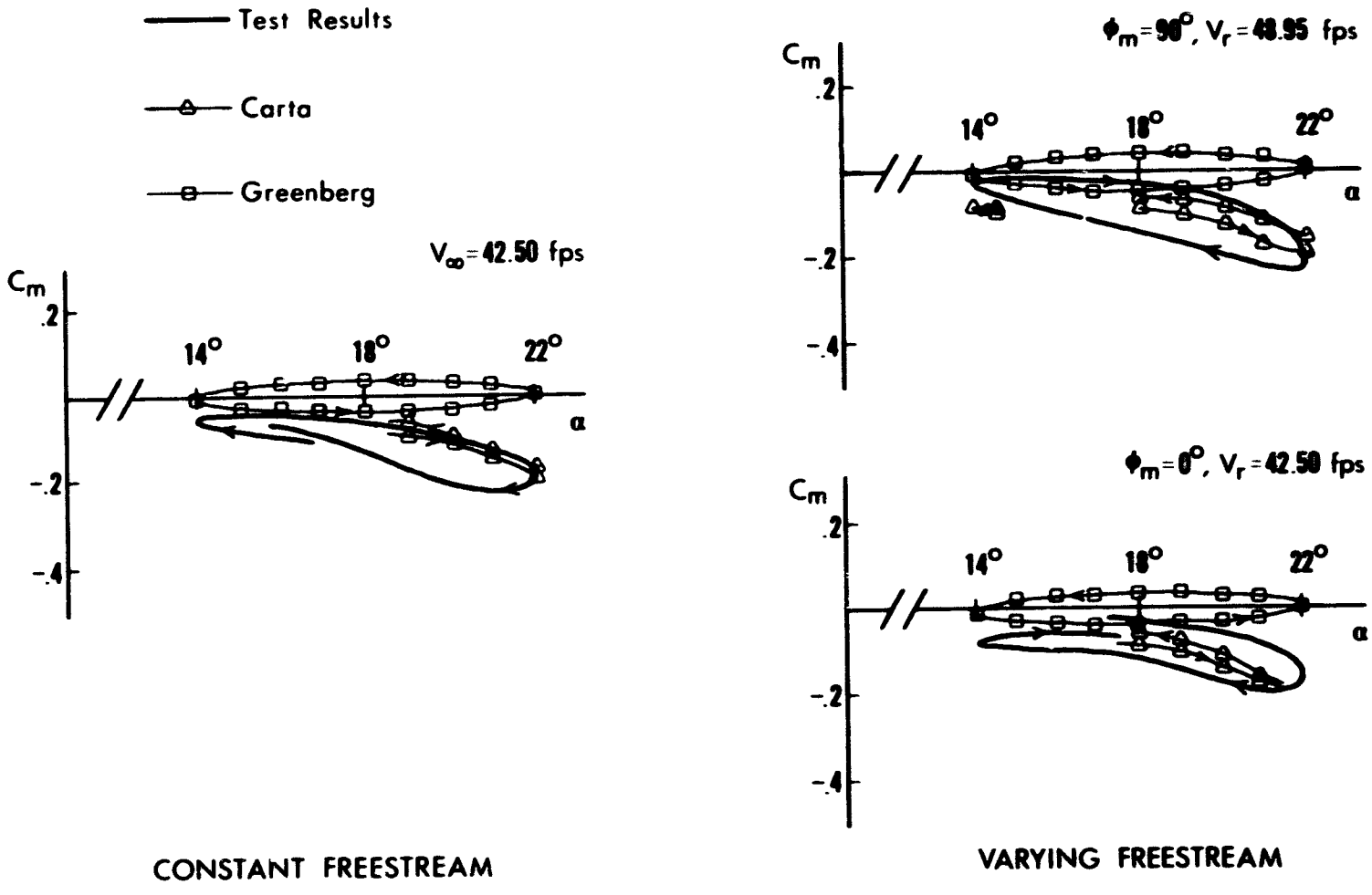

Figure 29. Analytical and Experimental C_m vs. α for Oscillations About 18° at 6 Hz in Constant and 1 Hz Varying Freestreams

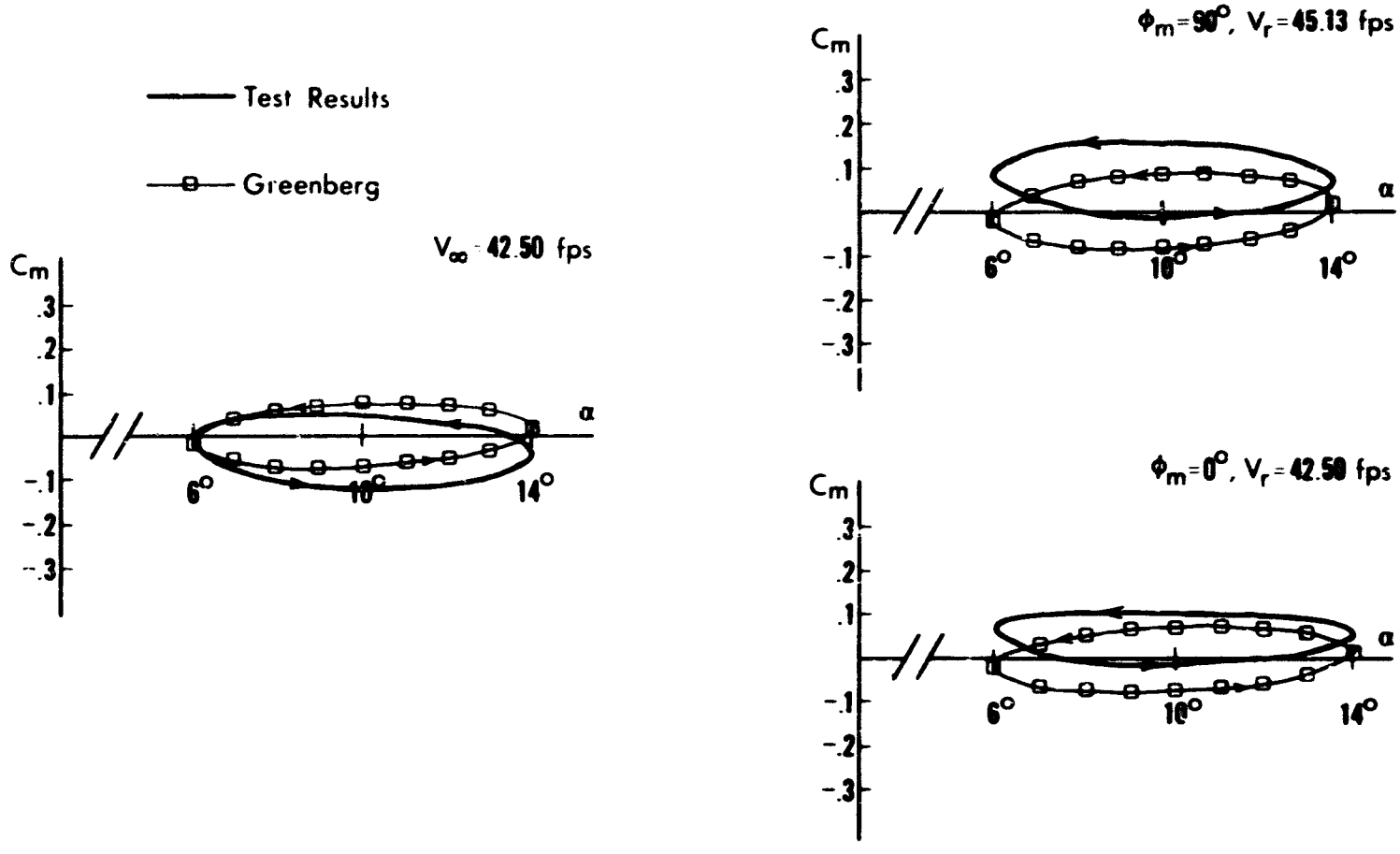

CONSTANT FREESTREAM

VARYING FREESTREAM

Figure 30. Analytical and Experimental C_m vs. α for Oscillations About 10° at 12 Hz in Constant and 2 Hz Varying Freestreams

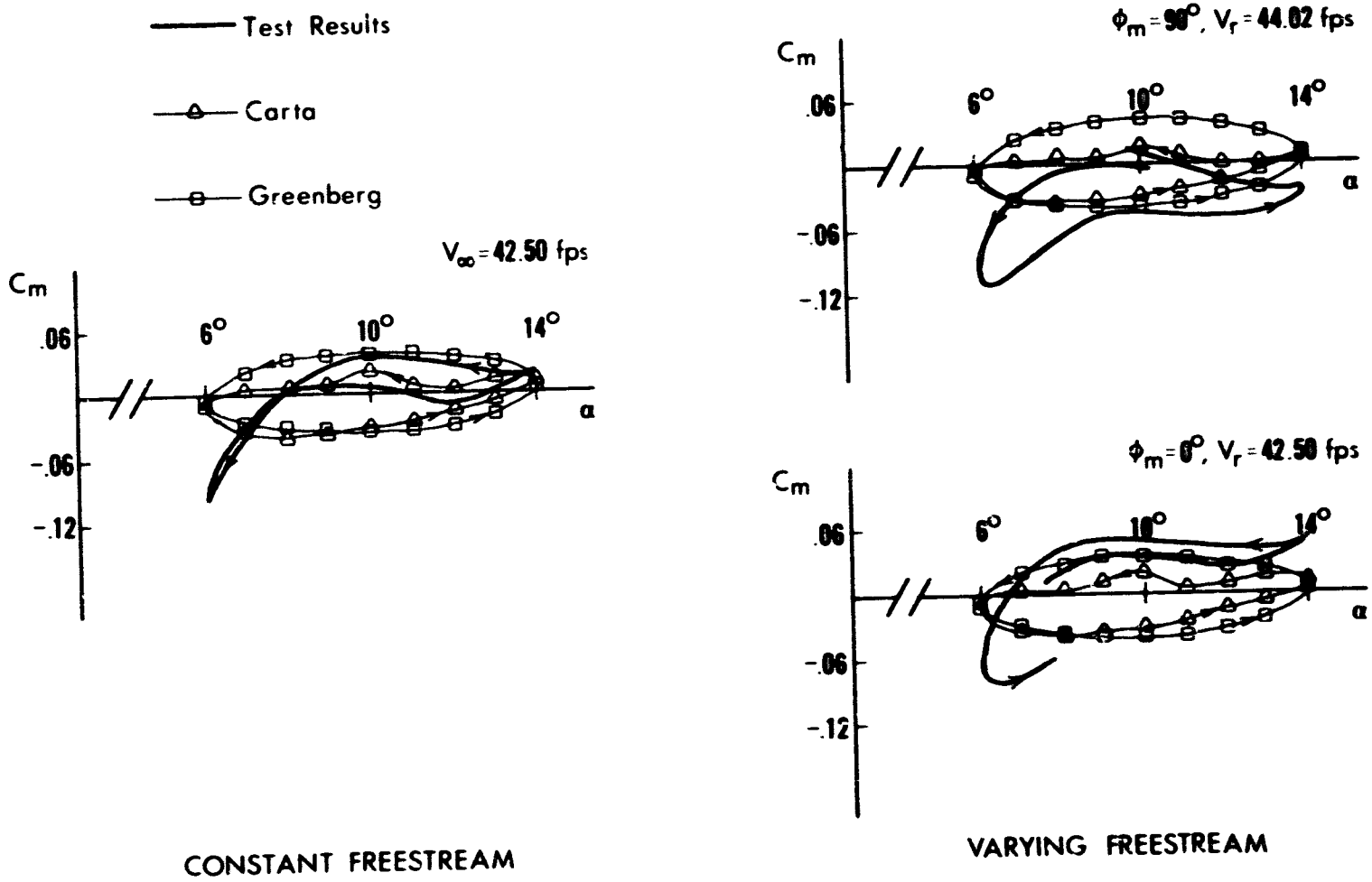

Figure 31. Analytical and Experimental C_m vs. α for Oscillations About 10° at 6 Hz in Constant and 2 Hz Varying Freestreams

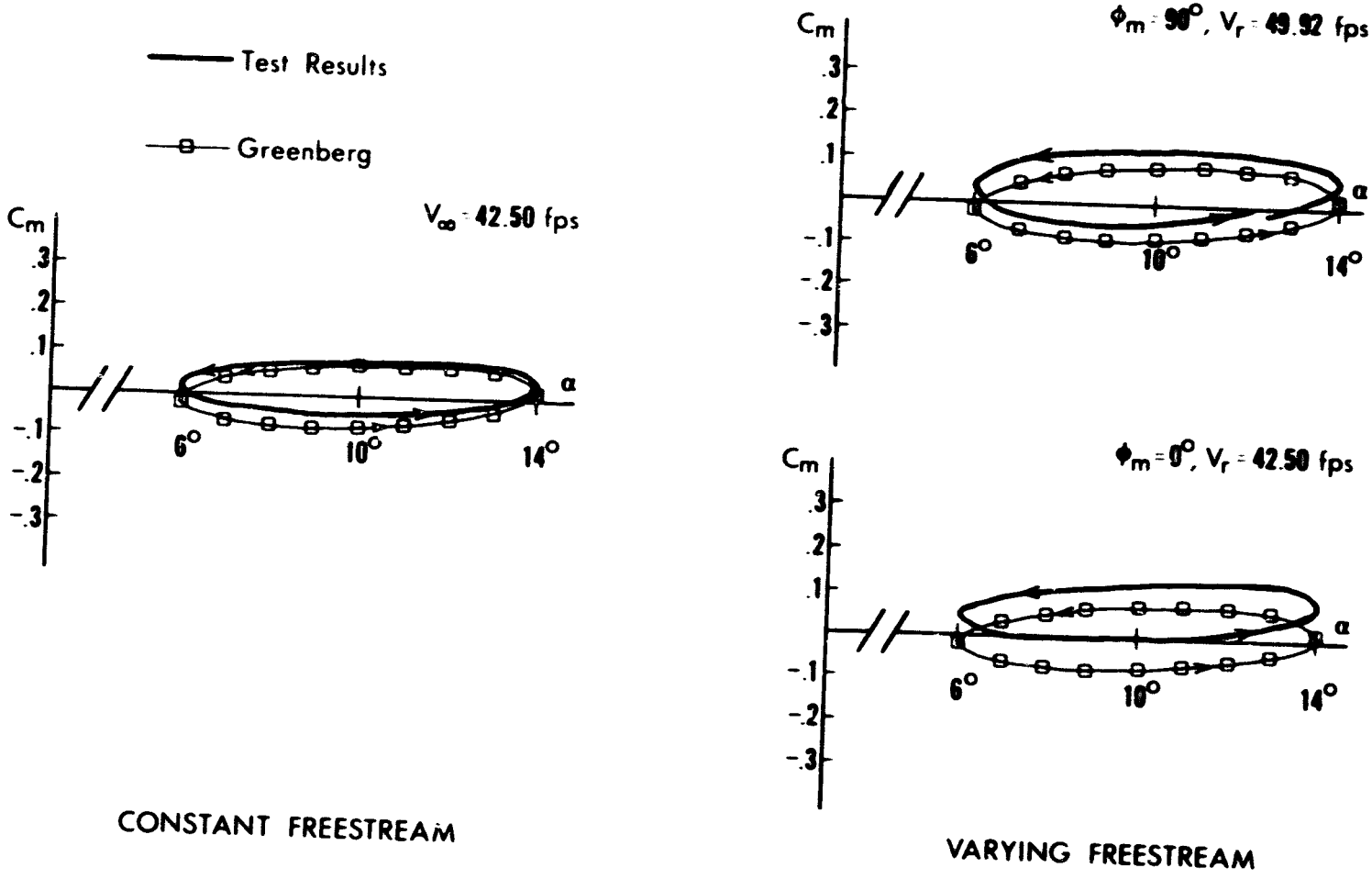

Figure 32. Analytical and Experimental C_m vs. α for Oscillations About 10° at 12 Hz in Constant and 1 Hz Varying Freestreams

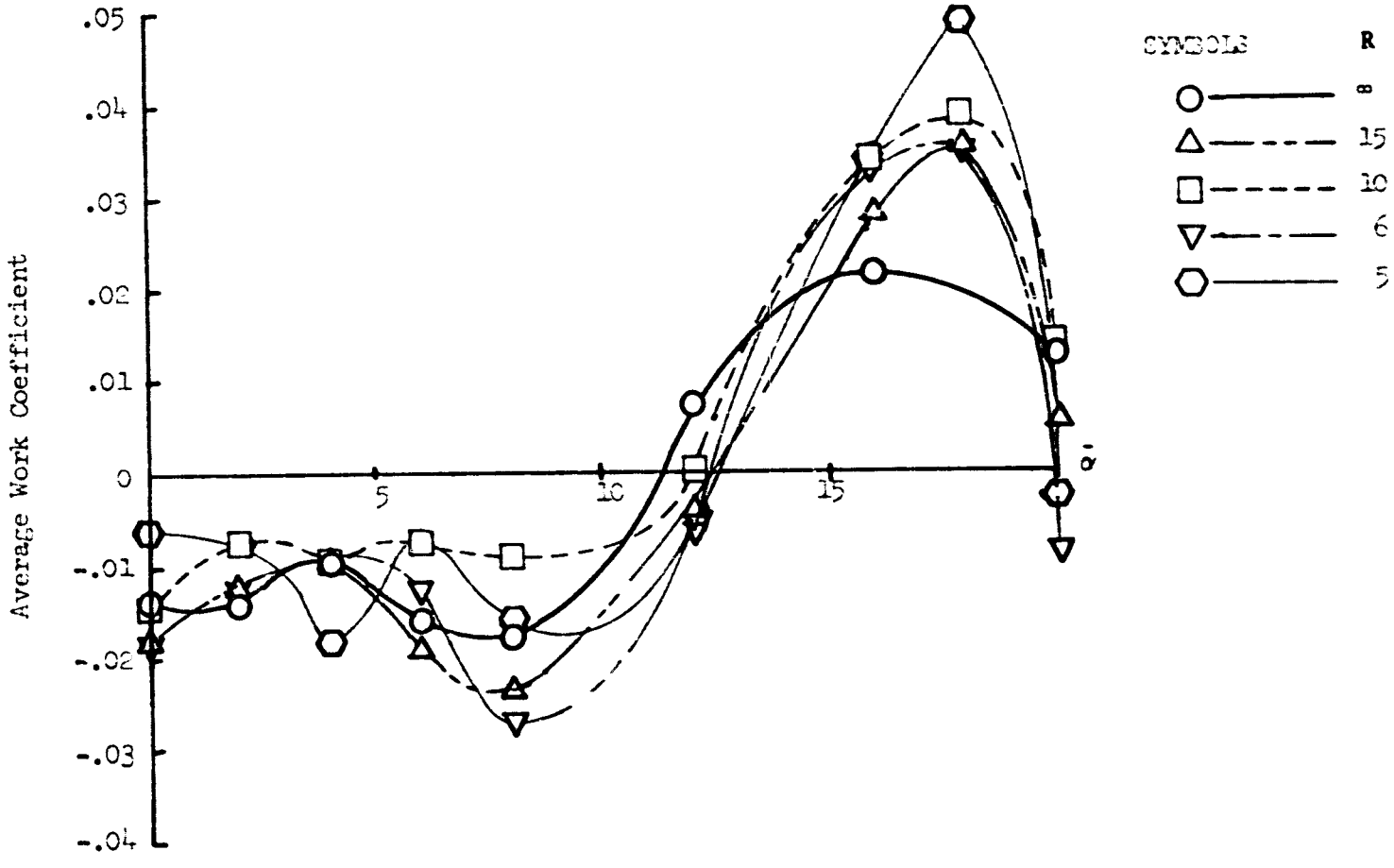

Figure 33. Work Coefficient Versus Mean Angle.